FACULTY
OF MATHEMATICS
AND PHYSICS
Charles University

MASTER THESIS

Jaroslav Knotek

Automation of nuclear fuel visual inspection

Department of Software and Computer Science Education

Supervisor of the master thesis: RNDr. Jan Blažek, Ph.D.

Study programme: Computer Science

Study branch: Software and Data Engineering

Prague 2020

I declare that I carried out this master thesis independently, and only with the cited sources, literature and other professional sources.

I understand that my work relates to the rights and obligations under the Act No. 121/2000 Sb., the Copyright Act, as amended, in particular the fact that the Charles University has the right to conclude a license agreement on the use of this work as a school work pursuant to Section 60 subsection 1 of the Copyright Act.

In Prague date May 27th 2020   signature of the author

Title: Automation of nuclear fuel visual inspection

Author: Jaroslav Knotek

Department: Department of Software and Computer Science Education

Supervisor: RNDr. Jan Blažek, Ph.D., Department of Software and Computer Science Education

Abstract:

The safety and performance of nuclear plant relies, among others, on the quality of nuclear fuel. The quality fulfilling designed criteria of the fuel in use is inspected and reported on periodically. Visual inspection focuses on the condition of the fuel based on its visual properties. During the inspection, the fuel is being recorded and analysed by the inspector. The current state of the fuel assemblies is compared to the historical statistics which helps do decide whether this particular assembly remains or gets replaced. This thesis describe a project initiated by Centrum Výzkumu Řež focusing on digital image processing methods application to visual inspection process. The result of the project is a tool that accelerates the process of report making. Firstly, it transforms the inspection video into one image overview and highlight a significant part (more than 95%) of possible defects to the inspector.

Keywords: Computer vision, Nuclear fuel, Automation

Contents

List of Abbreviations

OIO   One Image Overview

CED   Canny Edge Detector

FA   Fuel Assembly

POC   Proof of Concept

ROI   Region of Interest

SG   Spacer Grid

FR   Fuel Rod

HSV   Hue, Saturation, Value color model

CVR   Centrum Výzkumu Řež

FDDM Fuel Defect Detection Method

RAIP Row Average Intensity Profile

RSIP Row Sum Intensity Profile

CAIP Column Average Intensity Profile

CSIP Column Sum Intensity Profile

DIP   Digital Image Processing

ANN   Artificial Neural Networks

1. Introduction

This thesis describes a project focused on an automation of nuclear fuel inspection realized on the reference to the Centrum Výzkumu Řež (CVR) and describes methods applied in the process. The inspection plays a crucial role in nuclear fuel life-cycle, it ensures reliability and safety of the fuel, preventing incidents resulting from it's undesigned behavior. The main subject of such inspection is Fuel Assembly (FA) shown in Figure 1.1. During the inspection various measurements can be performed: physical deformations assessed by ultrasonic or laser based methods, eddy-current examination checking the surface of the fuel rods [1] and a human-based visual inspection.

Figure 1.1: Russian type of Nuclear Fuel Assembly arranged into hexagon. This picture shows the main parts of visual inspection: fuel rods and spacer grids. In the picture, few rods are extracted to reveal the inner structure. The other parts of the assembly are not pictured for clarity. (source CVR)

The visual inspection in CVR is performed manually by the team of two people: the camera operator and inspector. The camera operator screens FA while the inspector is watching the video simultaneously, closely examining the presence of fuel defects. The visual inspection takes place annually while the nuclear reactor is down. During the inspection, only a sample of FA are inspected - each is inspected individually [2].

The inspection videos can show only the peripheral fuel rods, the rods inside are not visible to the inspector. They are not inspected visually, their state is predicted from the state of the visible ones. The result of the inspection is summarized in a report which contains data of all encountered defects stating whether the assembly can be reused (possibly with repairs) or needs to be replaced with a new one. The report contains images with all defects detected in a form or manually composed One Image Overview (OIO). The typical situation is that all anomalies found are within designed acceptance.

It is essential to properly define the word defect. In the nuclear fuel inspection terminology, the word "defect" refers to a deficiency which discards FA from

future use. Throughout this work, the word defect refers to deficiencies which require attention of the inspector who documents it and assess its severity.

The central topic of the project was to research into the possibilities of automation using Digital Image Processing (DIP) methods. The activity most suitable for improvement was the report making. Our idea was to generate OIOs automatically from the videos and highlight all defects. This OIO can be immediately used by the inspector for quick overview and as evidence in the report making. The inspector is then not required to go through the whole video to locate any particular defect - the whole video content is shown in OIO instead. This information contraction has the following impact:

- It significantly reduces data processing time after the inspection.

- It lowers the possibility of a human error caused by subjectivity or fatigue.

This thesis present Fuel Defect Detection Method (FDDM) developed (by the author and his supervisor) during three months of implementation. Our target was to create a Proof of Concept (POC) for a task automation and defect detection based on visual inspection videos. Such videos would require a change in the screening process. So far, the inspection videos contain interruptions e.g the camera stops to zoom in on a one place or returns to some previous locations. Such parts would interfere with the design of FDDM and their recording was part of this project as well.

The development went through three major iterations in which the recording scene significantly improved—leading to consequent adaptation of FDDM (such changes are discussed in detail in Section 3.4). At the end of the project, the results of POC were asserted by CVR and the project continued.

2. Related Work

The goal of visual inspection is to asses overall condition of FA, its defects and their properties. The possible defects range from construction deformations (bending, twisting) to corrosion and hydridation to debris and deposited materials. The inspection should statistically reveal overall condition of the fuel inside the whole reactor. Due to the limited time reserved for each inspection session (between 70 and 120 hours annually [3]), only sample set of all FA in the reactor is inspected.

The visual inspection focuses on defects ranging from chemical based on surface spots to physical deformations (such as bow or twist) or cladding damage (scratches, debris fretting or grid-to-rod fretting)[4; 2]. In this thesis, we focus only on the spots, scratches and debris. The physical deformations were out of scope of this POC.

Some level of defect is acceptable [2], for example—the oxide layer can be commonly encountered but if not checked regularly, it can grow and form a solid layer of corrosion which can peel off and deposit somewhere and it can eventually lead to the cladding degradation and consequent fuel leakage. Such defects can be seen in Figure 2.1. Such situation is prevented by the visual inspections.

According to Martina Mala [5], the inspection is performed on a dedicated mobile-inspection-stand which is assembled in the reactor hall before each inspection session starts. The stand has a camera with a dedicated light for visual inspection and a ultrasound device for leakage inspection.

The nuclear fuel inspection procedure is unique to each facility but what applies to all of them is human expertise. Due to the severity of a possible incident, it is the inspector who makes final decisions which is based on the specifics of the defect found, its historical data and the expertise coming from the community of inspectors. In the field, the automation tools are used only for the most tedious manual work and as a support for decision making. One such example is a nuclear fuel defect detection based on deep neural networks [6]. Authors collect the dataset in the experimental facility training the neural network to recognize and locate scratches. The article mentions no real application and results on real data.

Artificial Neural Networks (ANN) were not used in our part of POC. The goal of this project was to highlight all defects and let the inspector decide their severity. Which means that FDDM was designed to maximize precision and measure recall. Due to the conservative approach of the inspection, it was acceptable to have some false positives in the results as long as all severe defects had been included. ANN, on the other hand, are used for the tasks where the precision is the primary goal. In some tasks, ANN can achieve very high precision. The main requirement for this is a reliable and credible dataset. Having a good dataset and model is still not a guarantee of success. The process of ANN calculation is not transparent therefore incorrect results could be corrected only by improving the dataset.

Even though the ANN dominates the DIP field, some tasks suits better to traditional techniques. One such example is defect detection performed on train rails done by Min et al. [7]. Min's approach has similarities to the one described in
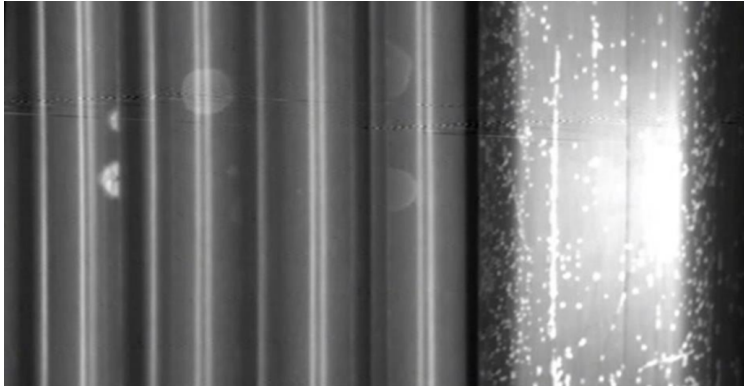
(a) Oxides [3]

(b) Corrosion [4]
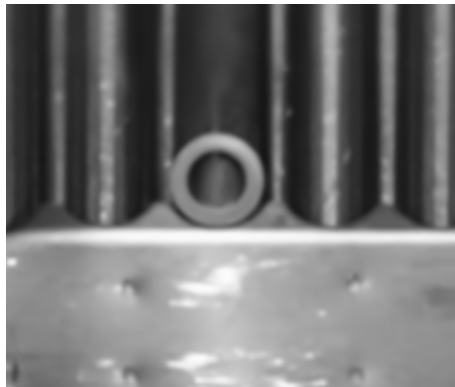
(c) Debris

Figure 2.1: Figure 2.1a depicts the real oxide spots that appears on the surface of the assembly. If left to grow, it can lead to corrosion shown in Figure 2.1b. The corrosion is the state that must be avoided since it can severely damage the cladding fuel rods leaving a hole behind or peel off and deposit somewhere. Any foreign object or debris can cause fretting that leads to damage of the cladding. Debris seen in Figure 2.1c needs to be located and removed.

this thesis. To achieve high quality dataset, Min build own screening equipment and extract features from regular environment (also recorded on a video) with the pipeline consisting of the following stages:

- Cropping frame to Region of Interest (ROI) using variance of image parts

- Image enhancing

- Actual defect detection

The results are then presented to the inspector who then takes decision. The failure rate of such method is close to 5 % and the shortcoming of this method is its sensitivity to uneven light which needs to be reduced in the future. In our case, the problem is also well defined e.g. to locate white spots or (usually) dark debris. The initial idea was to try straight forward DIP that will correspond to the already well established methods of visual inspection. DIP methods proved suitable for this type of task. DIP is suitable for defect with straight forward visual properties. ANN would be better for defects having visual properties well defined.

The nuclear fuel inspection specifics are considered trade secret therefore details of the process of inspection are not made public. Due to this fact, the number of references cited in this chapter and the level of detail of the the inspection process is very limited. This project was driven by work and consultation with Marcin Kopeć, Martina Malá and papers [5; 2; 3].

3. Problem analysis

The goal of this chapter is to introduce the main characteristics of FA and its possible defects (Section 3.1) followed by the detailed description of the experimental facility which had a special scene equipped for recording of the mock videos (see Section 3.2). The impact of the scene on the videos is described in detail in Section 3.3. The outcome of this project was the design of FDDM as well as the setup of screening process. The process of development consists of the multiple iterations explained in Section 3.4.

3.1 Characteristics of Fuel Assembly

The subject FA is 1.5 m tall used in experimental reactors (nuclear plants have FA which is around 4.5 m tall), it consist of 312 Fuel Rod (FR) organized into hexagon by several Spacer Grid (SG)s. The number of SGs or distances between them were not important to the method and can be neglected. Both FRs and SGs are made of zircon alloy that visually resembles stainless steel. Each side of the FA has 11 parallel and equidistant peripheral FRs with approximately 4 mm wide gap and a single rod is 10 mm wide. SGs can be slightly tilted within acceptable limit $\pm 7.8°$. The surface of SG is flat and may have some text engraved. In our case, there are 10 teeth on the top and 10 on the bottom with some exceptions whens some SGs can have only 9 teeth because they have a groove in the middle of both top and bottom edges. The detail of spacer grid can be seen in Figure 3.1.

We are simulating two types of defects: oxides and debris. The oxides are white spots that vary in shape and size and can be surrounded by a gray film (the gray film is considered defect). The oxides are simulated with white marker and appear only on FR. Debris is any foreign object for example, a short wire or a bolt. The debris is typically located near SG. The comparison of the real and simulated oxides can be seen in Figure 3.2.

3.2 Scene Characteristics

The videos used in this project were taken in the experimental facility. The real inspection scene was simulated using a water tank, a custom-made camera-stand
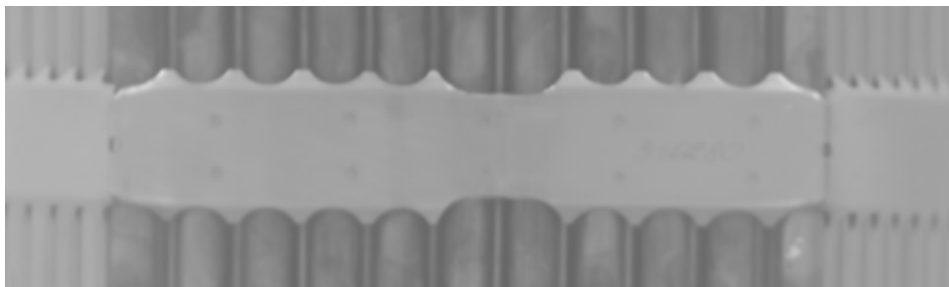
Figure 3.1: The image shows the detail of a spacer grid. On the top and bottom there are teeth enclosing fuel rods. A groove is on the top edge between the seventh and eight rod. There can be a number engraved on the right side.
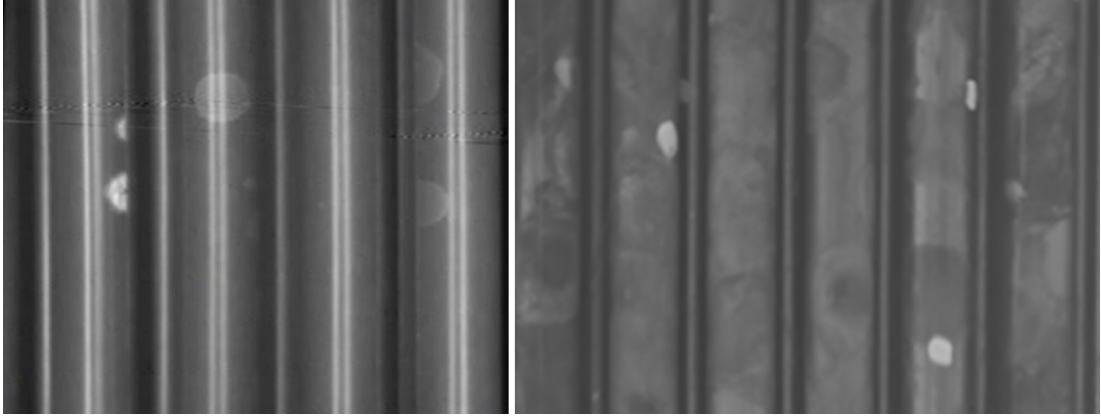
Figure 3.2: The real oxides on the right side versus the simulated oxides on the right. They are created by applying white correction marker.

and a real version of FA. In later stages of the development, the water in the tank was dyed with milk to simulate potentially impure in the spent fuel pool and to reduce the reflections. The custom-made camera-stand consists of two parts: the first part stands outside of the water tank and its robust construction stabilizes the camera grip, reducing its shaking. The other part consists of a motor which extends a pole on which the camera is attached. The camera is held underwater approximately 40 cm from FA and moves vertically along from top to bottom. The equipment used for FA screening is shown in Figure 3.3

3.3 Video Characteristics

Each video is around one minute long and shows two top-down passes along FA (we utilize only a single top-down pass). The initial videos were recorded by an action camera - Easypix GoXtreme Race Mini with full HD resolution and the camera parameters adapt automatically to the environment and cannot be set manually. Although this camera was replaced in the second iteration of the project (see Section 3.4), the method remained the same and still could handle the videos from both cameras (for the parameters of the camera, please refer to Appendix A). The videos recorded by both cameras have the characteristics described below. The example frames can be seen in Figure 4.5.

The camera is moving along FA at constant speed. It ensures that the the area of FA covered by every two subsequent frames is equally distanced (this observation is leveraged in Section 4.4). The camera and stand are controlled separately so the video contains parts where the camera stays still. Such parts would interfere with the method and are removed manually.

The videos show one frontal side of FA and two adjusted sides The adjusted sides are not important for the purposes of the inspection since - they are inspected in it's own video therefore they can be removed. There are two options how to crop them: bringing camera closer to FA or removing the adjusted sides algorithmically. The former option would require better, wide-angle, objective because the current one would cause significant fish-eye distortion and their videos

9

(a)
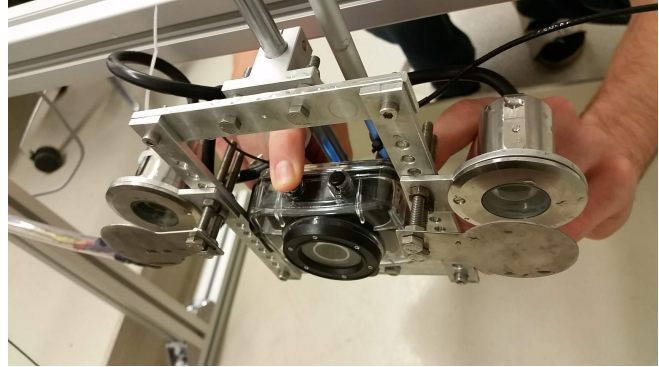
(b)
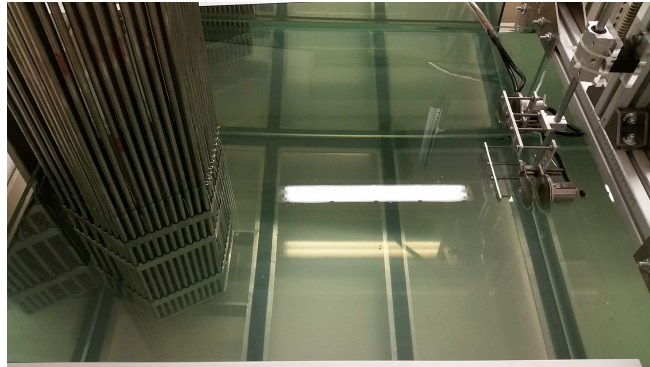
(c)

Figure 3.3: In Figure 3.3a, we can see the water tank, camera-stand with the robotic arm and FA used for screening. As we can see, FA is taller than the water tank therefore only a part of it (around 60 cm) is under water and therefore it is subject of recording. In Figure 3.3b, we can see the detail of the camera and the point-light source, both attached to the robotic arm. Figure 3.3c shows the setup prepared for the screening.
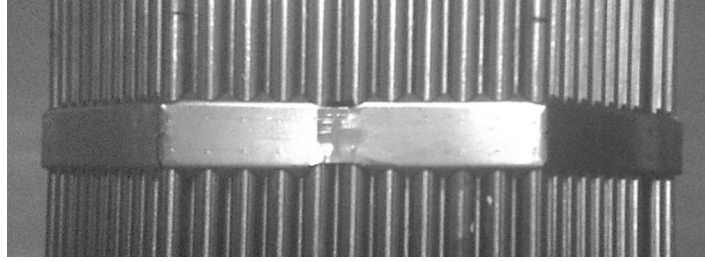
(a)
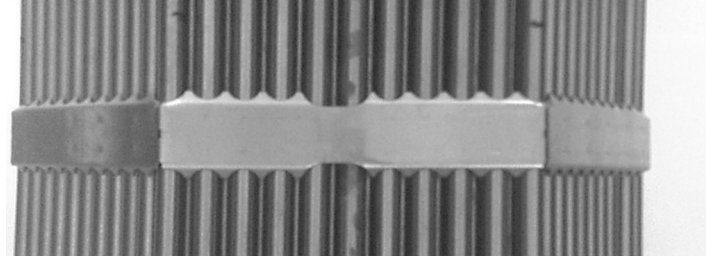
(b)

Figure 3.4: The comparison of the illumination types. Figure 3.4a shows point light. We can see the sharp reflections on the surface of the rods, between them and on the spacer grid. The image appears significantly darker and rather blurrier than the frame from tube-light in Figure 3.4b. There we can see more equally distributed light and the sharper edges of the spacer grid.

are blurred (example frame can be seen in Figure 3.5). The second option was selected since it was closer to the currently used camera which has the resolution of 800x600 while the camera used in mock screening was full HD. Placing the camera further away (distance was around 40 cm because it was limited by the water tank size) firstly lowered the resolution of area covering FA to about a half of the frame width and secondly reduced the fish eye effect affecting the borders of the image.

The frames are slightly rotated. The rotation is caused by imprecise attachment of the camera to the stand. To improve the robustness of the method and because the rotation is the same in all frames(max ±4°), the rotation is normalized algorithmically instead of levelling the camera manually.

NFA is screened under two different types of light. Our dataset comprises of two major groups of videos differing in an illumination type. The first group consists of the point-light illuminated videos that are supposed to represent the illumination found in the real inspection videos (in the beginning they were not but their quality gradually improved with the development). In this case, the light is moving with the camera. The other group contains the tube-light illuminated videos used for testing purposes due to their better quality and the light source is the tube under the room ceiling hence "tube-light". The goal was to improve the point-light to the level it would be as close as possible to tube-light videos. The example frames from both type of videos can be seen in Figure 3.4.
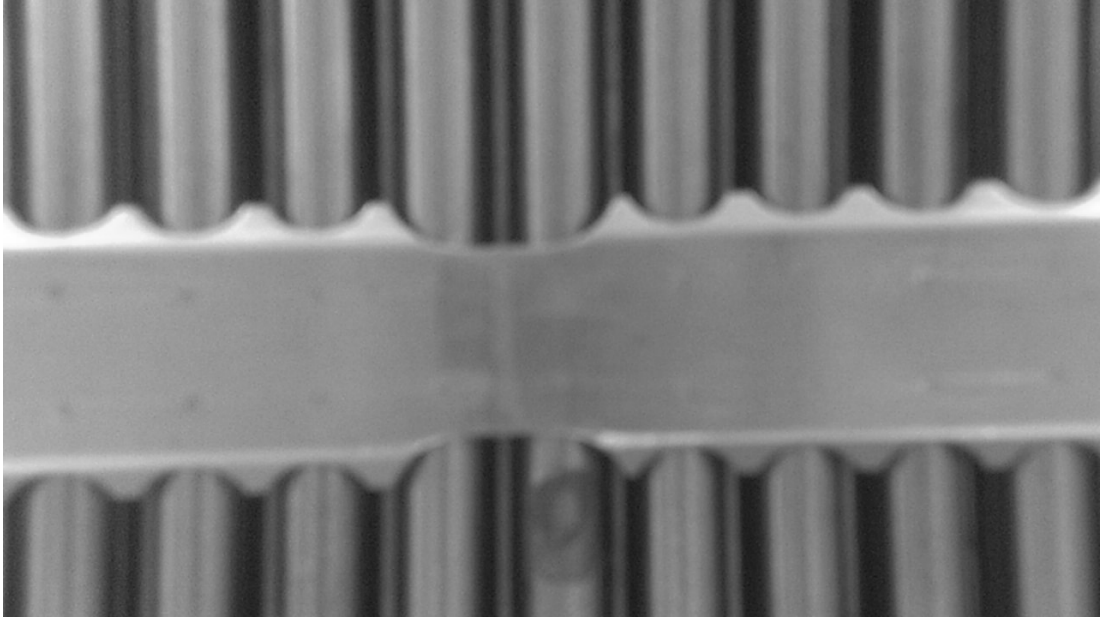
Figure 3.5: The first group of videos were zoomed in on the fuel rods of frontal side. The example frame presented here is very blurry and generally unusable for our cause.

3.4   Project Iterations

For better understanding of crucial aspects of the project (two types of light, method's results influencing the scene etc.) it is important to know the progress and the events that influenced the course of the development. The development was done iteratively, during 3 months, where each iteration begun with a set of videos recorded, then the method was adapted and its results assessed. Some poor results could be attributed to the insufficient quality of the data. In such case, the scene was adapted to fit the new requirements and new iteration began.

Iteration I   At the beginning of the first iteration, two types of videos were recorded. The first videos were zoomed in on the rods of FA, as was done in the real inspection (see Figure 3.5). Such videos were very blurred and affected by the fish-eye effect. Due to their low quality, the method-in-development could not achieve any results even with the absolute basic tools such as edge detection. The other submitted group consisted of videos recorded under tube-light. The tube light videos represent the desired quality of the point-light videos that were being recorded at the time. At the end of this iteration, despite the fact that the camera was shaking and tilted, the overall quality was sufficient and first visible results in OIO composition were achieved (see Figure 4.12).

Iteration II   The point-light videos were submitted in the second iteration. The videos were generally very dark with very sharp reflections and low signal to noise ratio. Example frame from such videos as was presented in Figure 3.4a. The shakiness of the camera persisted even though some efforts to reinforce the stand had been made. It was necessary to improve the stability even more and the development of the new stand commenced.

Iteration III   The last iteration started with three major improvements:

- The reinforced camera-stand was finished - The parameters described in Section 3.2 remained the same therefore the method did not have to change at all. The final form of the camera stand can be seen in Figure 3.3.

- A new camera was bought - the original camera was replaced with Olympus IM005 (for more detail please refer to Appendix A). The Olympus camera was larger and heavier countering the camera-stand reinforcement therefore some shakiness remained observable.

- Point-light videos improvements - The point-light lamp was equipped with diffusion filter which reduces the sharpness of the reflections. The improvement was also affected by the dynamic range of the new camera. Altogether, the quality of the point light videos approached the quality of the tube light ones.

Each iteration brings improvements on both sides - the scene and method. The scene started with the low-tier camera, sharp light, a shaky stand and ended up as a solid environment for good quality videos (however, same aspects of the scene could be further improved e.g. point-light screening). The increasing quality also impacted the development of FDDM. Although the importance of some features of the pipeline was decreasing with each iteration, they were not removed for sake of robustness required in the real environment. Due to that, the pipeline, at the end of the project could process the videos from all iterations; even though the main focus was on the latest videos.

This thesis aims to test DIP methods for the purposes of FA screening performed during the real inspection. In this chapter, the characteristics of FA and the scene were presented. The scene was designed to follow the real screening conditions from the nuclear power plant. The iterative development of this project resulted in a robust pipeline described in the next chapter which has a potential to optimize the inspection process.

4. Method

FDDM is composed as a pipeline with the three stages below (also shown in Figure 4.1). Each step depends on the quality of the predecessor. If any step fails or produces malformed output, then the remaining step also fails.

- OIO Construction - Transforms input video into OIO

- Fuel Inspection - Performs segmentation and defect detection. A point illuminated OIO is treated differently than tube illuminated OIO (discussed in detail in Section 4.2).

- Visualization - Post-processes detected defects and highlight then on OIO
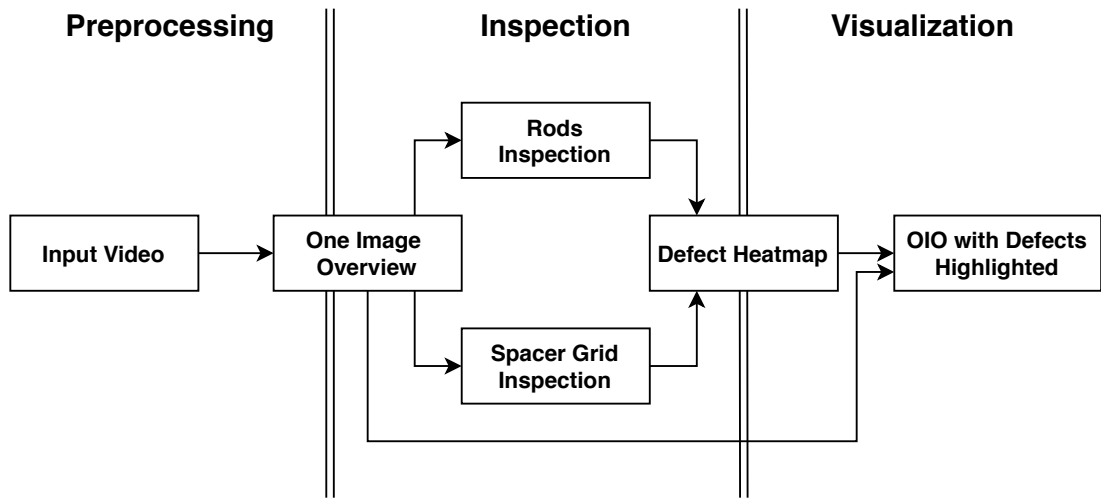
Figure 4.1: The diagram shows the three stages of the pipeline: OIO construction, Fuel inspection and Visualization. Each stage works with different imagery. OIO construction stage turns video into OIO. Inspection stage turns OIO into segments, then to defect heatmap and finally the Fuel Visualization combines defect heatmaps with the original OIO and produce OIO with defects highlighted

4.1 Notation

The following notation is frequently used in the text:

- Image is a continuous bilinear approximation of a raster of pixels $I^{(W*H)}$ where $I = [0, 1]$ denotes intensity, W is raster width and H raster height

$$img : [0, W-1] \times [0, H-1] \to I, img(x, y) = i$$

- ROW_y^{img} is a function that for a given Image img and a given coordinate $y \in [0, H-1]$ returns a row of the image.

$$ROW_y^{img} : [0, W-1] \to I$$

$$ROW_y^{img}(x) = img(x, y)$$

14

- COl_x^{img} is a function that for image img and $x \in [0, W-1]$ return a column of the image.

$$COL_x^{img} : [0, H-1] \to I$$
$$COL_x^{img}(y) = img(x, y)$$

- R denotes Row Average Intensity Profile (RAIP) (see Section 4.2) which has the same range and dimension as ROW of image img where

$$R(x) = avg(COL(img, x)), x \in [0, H-1] \tag{4.1}$$

- C denotes Column Sum Intensity Profile (CSIP) (see Section 4.2) which has the same range and dimension as COL of image img where

$$C(y) = sum(ROW(img, y)), y \in [0, W-1] \tag{4.2}$$

- Frame f of input video is Image.

In the following text, we simplify the notation in such a way that in the context of the given image img, the notation ROW stands for $ROW(img, y)$ and COL for $COL(img, y)$. Additionally, RAIP denoted as $R(x)$ is referred to by RAIP only and the same simplification applies to CSIP.

4.2   Illumination Types - Comparison

In Section 3.3 we have introduced two types of videos found in the dataset: point-light and tube-light. The tube-light being of higher quality used for reference and point-light the one representing the light of the real videos. The example frames from both types were presented in Figure 3.4. The pipeline was designed to process both types of videos the same way. Due to the differences described below, one exception was made - cropping of the adjusted sides of FA (see Section 4.4). We expected that an universal algorithm which we did not have would not perform better. We decided to develop two specific algorithms for each type of light rather than develop the universal one.

The visual properties of FA can be presented in a form of a signal. We use two types of signal: CSIP and RAIP, each helping us characterize different set of properties. In the following text, we describe each type of signal how it it used and how it's properties are affected by the illumination type.

Column Sum Intensity Profile: CSIP (see Equation 4.2) is calculated as a sum of all rows across whole FA. It is used to locate boundaries in the spacer grids (see Section 4.5). Figure 4.2 shows the comparison of both types of illumination.

(a) Tube-light CSIP *(b) Point-light CSIP*
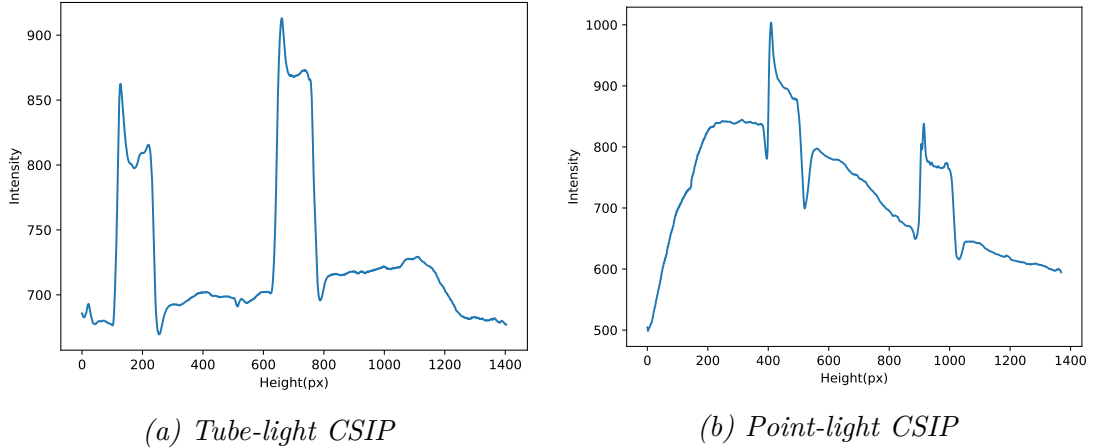
Figure 4.2: The spacer grids stand out at the first glance.

Row Average Intensity Profile of Rods: RAIP (see Equation 4.1) in this comparison is calculated from $ROWs$—representing the rods part (we utilize the information from CSIP to filter parts with SG out. For the clarity of the text, this step is described in detail in Section 4.5 - it is used there as a basis for more complex operations). Figure 4.3 shows the difference. Please notice that both images represent RAIP of not-yet-cropped OIO. We can see the interval from the left edge to approximately 180 px representing the background, then there is the part represents rods of the adjusted side (between 180 px and 350 px) and the middle part represents the 11 peripheral rods.

Row Average Intensity Profile of Spacer Grids: RAIP of SG is calculated from the rows representing spacer grids (extracted using CSIP the same way as in previous case). The comparison of spacer grids Row Sum Intensity Profile (RSIP) can be seen in Figure 4.4.

4.3 Applied Simplifications and Neglects

In order to solve the task given using DIP methods it is essential to limit the data complexity, ideally immediately when the data is collected. Based on the scene and input data observations presented in this section, the following simplifications are introduced in order to achieve effective and robust algorithms. All the neglects were discussed with CVR so the method would remain applicable in the real environment.

We expect that all defects are detectable in gray scale. This simplification enables disregarding triple-values RGB colour model in favour of a single value representing intensity.

The videos are properly cropped. Only the part of the video where the camera is moving is used for OIO composition. The other parts do not bring any additional information.
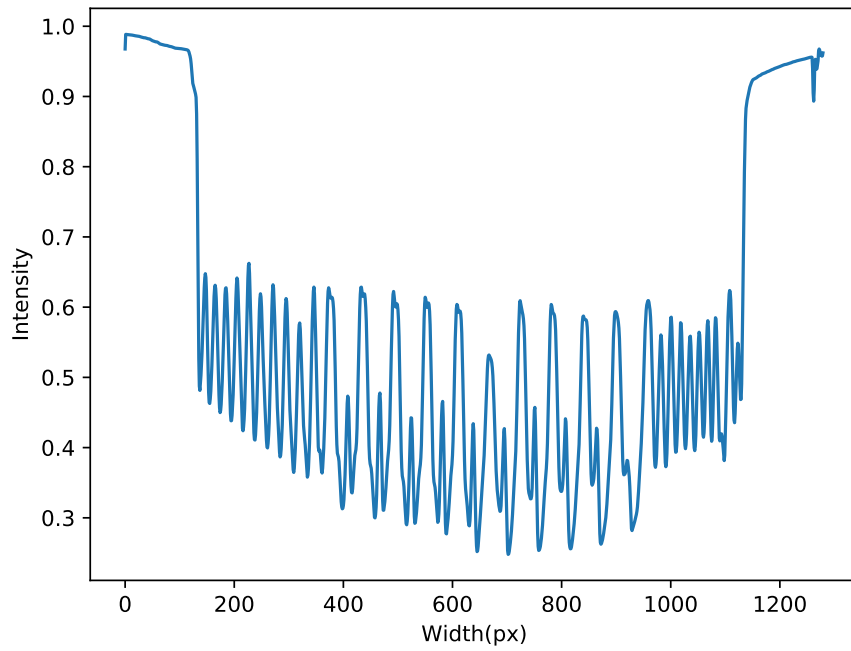
(a) Tube-light RAIP
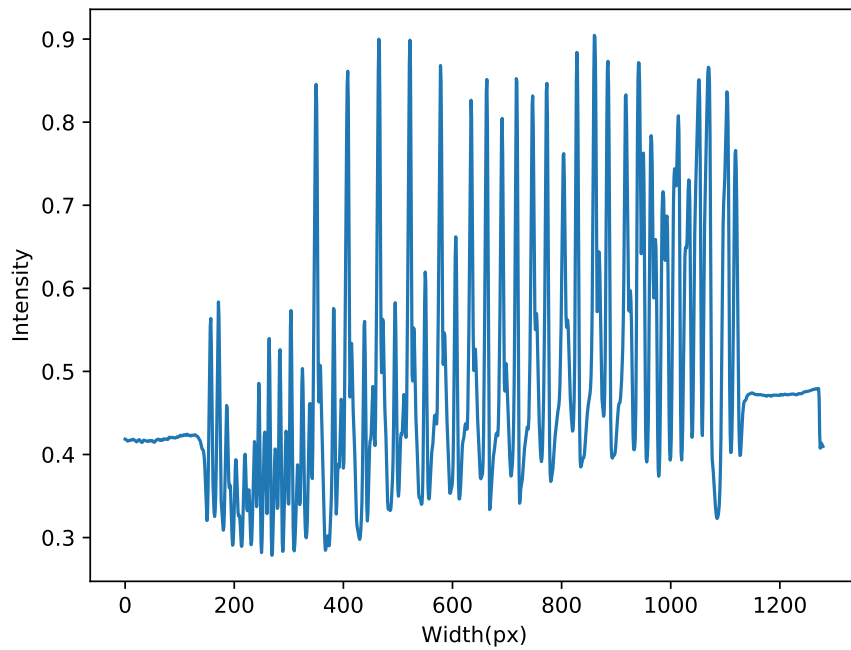
(b) Point-light RAIP

Figure 4.3: The tube-light RAIP 4.3a shows clearly visible signal of rods. Its periodicity reveals whether we are looking at frontal rods, adjusted side rods or the background which is flat. On the other hand, the point-light 4.3b does not display such structure.
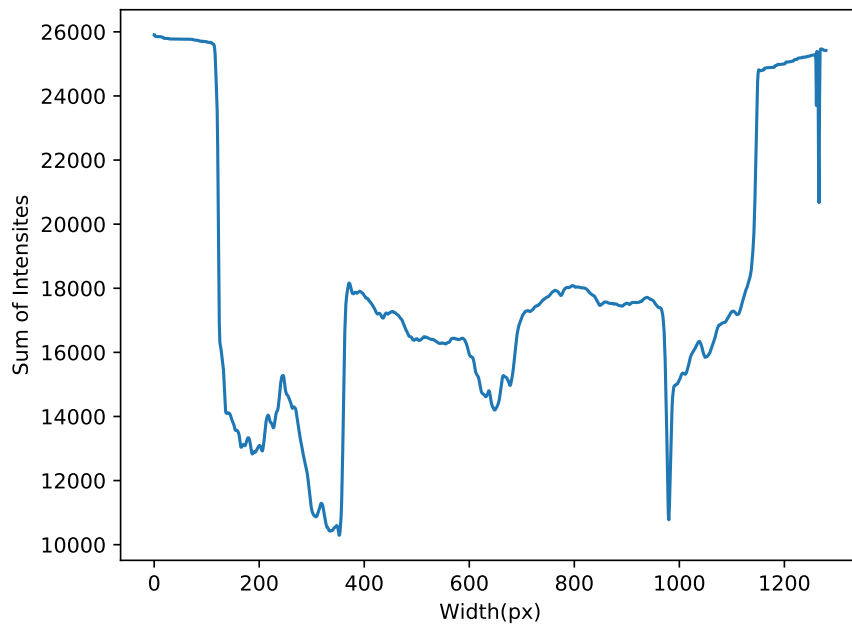
(a) Tube-light RSIP of spacer grids
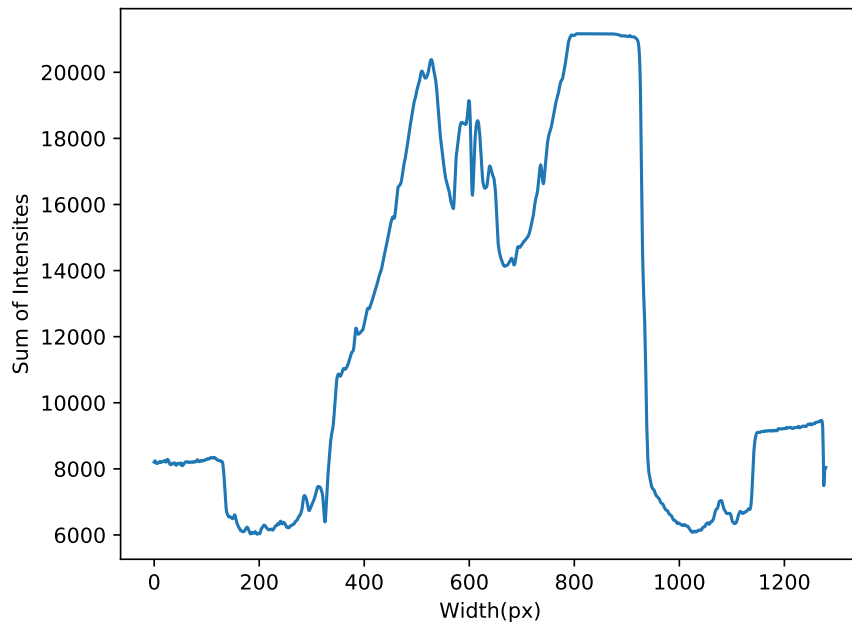
(b) Point-light RSIP of spacer grids

Figure 4.4: The point-light 4.4b spacer grids clearly reveal the boundaries of the frontal side (from around 400px to around 1000px). With this type of light, the difference between the dark background and very bright surface of the spacer grid is pronounced more significantly than in the tube-light RAIP 4.4a.
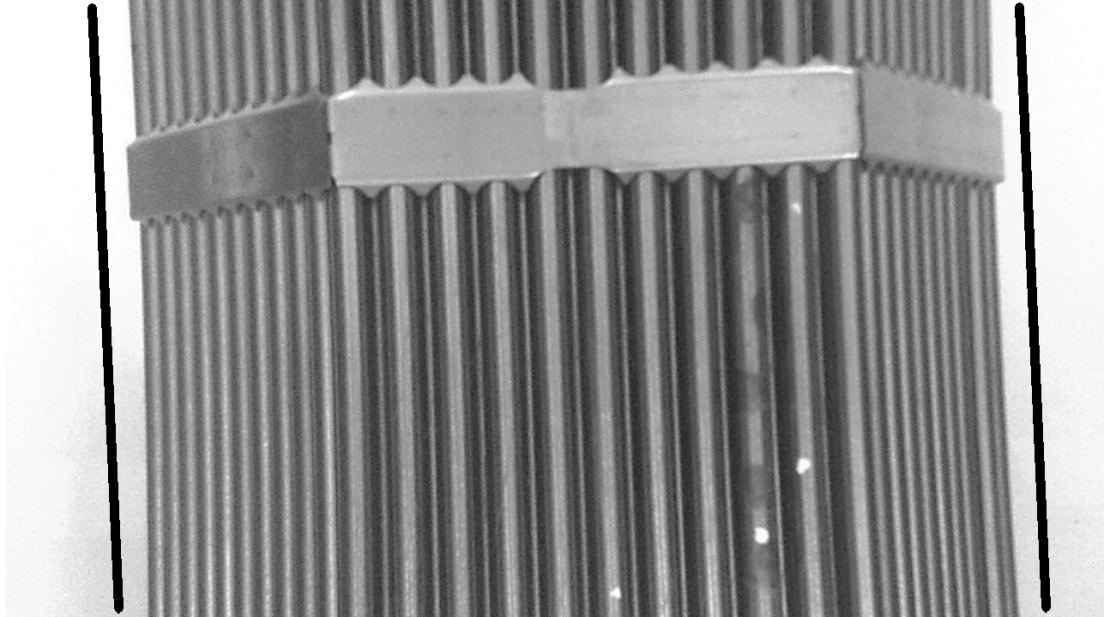
Figure 4.5: The frame shows NFA with three major regions. The frontal face with 11 rods and the spacer grid, The left and right adjusted sides and the background. The frame is visibly noisy and rotated by 7.5 degrees. The two black lines on the sides are in the same direction of NFA and helps to notice the fish-eye effect caused by the camera lens. The image shows white spots on the frontal rows that represents oxides.

The shaking of the is not taken into account. The effect of the shaking camera is almost not visible in the result, which greatly reduces complexity of OIO construction stage.

The distance from the camera lens to the FA is constant and the camera perpendicular to FA. With this simplification, the frames do not require normalization by perspective transformation and scaling.

The noise of the frames have approximately the same impact on all pixels. The expected noise distribution can be eliminated by averaging intensities of the same point captured by multiple frames (see 4.5).

The fish-eye effect is negligible in the central part of the frame It enable extraction of the undistorted central part of each frame (see Figure 4.6) instead of reducing the fish eye effect manually (e.g. by applying lens correction algorithms). The fish-eye effect is observable in Figure 4.5.

The distance between the camera and FA is approximately the same in all the videos. This simplifies the algorithms when working with the rods and grids (rods location, adjusted sides cropping etc).

4.4 Construction of One Image Overview

In this stage, as well as in the other stages, we follow this concept: The first part introduces assumptions about the content of the inputs. The assumptions
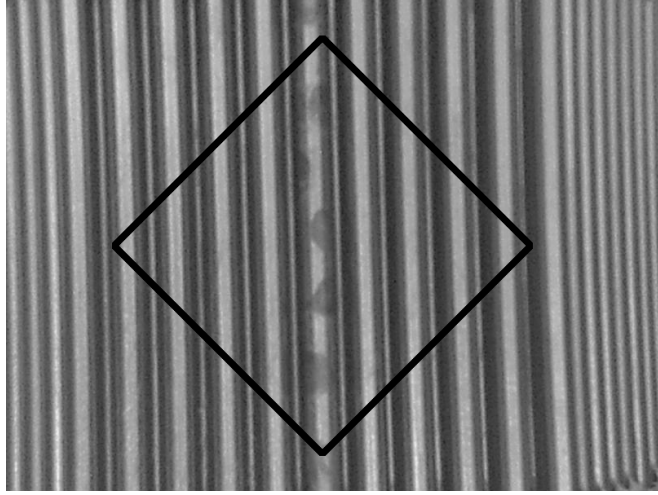
Figure 4.6: Central part of the frame is represented by the solid black diamond. The image is a close up of the actual frame. The width of a side is one third of the height of the actual frame.

are used in the hypotheses which are then asserted by the algorithms and then evaluated at the end of the section.

The goal of the OIO construction stage is to take video and compose OIO (see Figure 4.12 at the end of this section). The quality of this image has crucial impact on the results of FDDM therefore significant effort is put into compensation for the video shortcomings. The design of this stage is based on the simplifications made in Section 4.2 that were used to establish the following assumptions:

1. All frames can be rotated by the same angle *alpha* to normalize the rotation - Applying inverse angle rotation would normalize the rotation of all frames.

2. We neglect the fish-eye effect and use only the central part of the frame where it is not so strong. This leads to acceptable blurriness in OIO. - This part is used to properly register two subsequent frames onto themselves.

3. The camera-vertical-movement speed between two consecutive frames is around 2.3 px for Easipix and around 2.7 px for Olympus (given the different frame rate and constant distance between the camera and FA). The camera speed is used to calculate the offset between each two subsequent frames.

4. The noise of the frames has approximately the same impact on all pixels and affects pixels independently. - The noise can be canceled by averaging intensities of the same point of FA taken from multiple frames.

5. The image background is assumed to have approximately the same intensities(e.g. background is solid) therefore it can be removed by thresholding CSIP derivative C'.

6. FA has exactly 11 equidistant peripheral rods on the front side. Each two rods have a gap between them. This assumption is used for cropping the image to ROI.

7. In the image with FA without background, the top-left-peripheral-rod of the frontal-side lays between $\frac{1}{10}$ and $\frac{1}{5}$ of the width of the image. We use this assumption in case that the incorrect number of rods were found and we need find/discard the other.

Hypothesis: OIO can be created by normalizing rotation of each frame, cropping the parts unaffected by fish-eye and merging them together. Image is then cropped to ROI by removing the background and the adjusted sides. The result of this step would be OIO. The steps are visualized in the diagram seen in Figure 4.7.
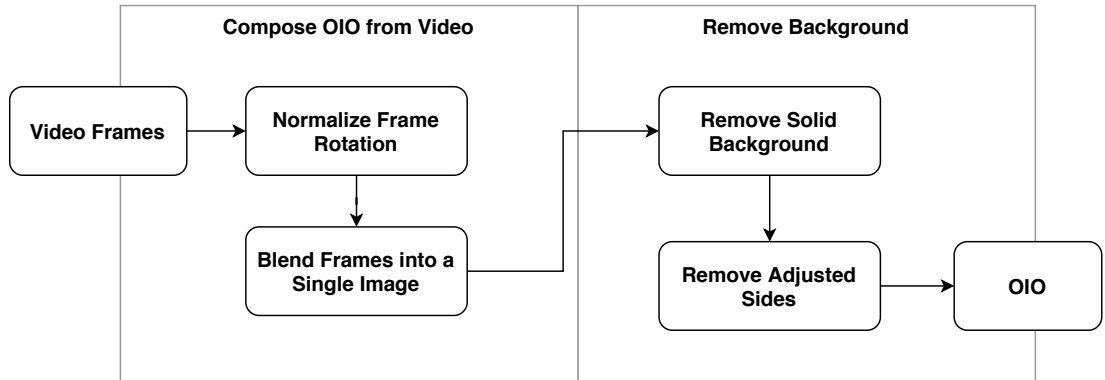
Figure 4.7: The diagram of the steps of the OIO construction stage (preprocessing) stage. It is subdivided into two major parts - the first is focused on OIO composition from video frames. The responsibility of the other is to remove the background.

Rotation Normalization

In the rotation-normalization step, the angle *alpha*, which all frames are rotated by (see Assumption 1), is calculated and its inversion is applied to each frame . all frames can be rotated by the inverse angle of α that represents the dominant direction of rods across all frames.

The direction of each frame cannot be calculated from the whole frame since its corners are affected by the fish-eye so the rods located there appear to be bent. Additionally, the frames cannot be normalized individually because some contain SG in the central part which prevents any direction extraction. Such frames are eliminated from the direction calculation.

According to Assumption 2, the rods in the central part of the frame f are straight and unaffected by the fish-eye. The lines, representing edges of rods and the straight reflections on the surface of the rods, are extracted by Hough Transformation [8].

The number of the lines found is different for each video but the goal was to set up parameters, preferably having rather more than less. But such preference can cause problems. Hough Transformation finds more lines for a single edge (see Figure 4.8) the lines are then averaged to get a single dominant direction. The angles of the lines extracted from one frame are denoted Θ. To mitigate the error caused by imprecisions, short lines were filtered out and the remaining one are averaged:

(a) Detected edges   *(b) Extracted lines*
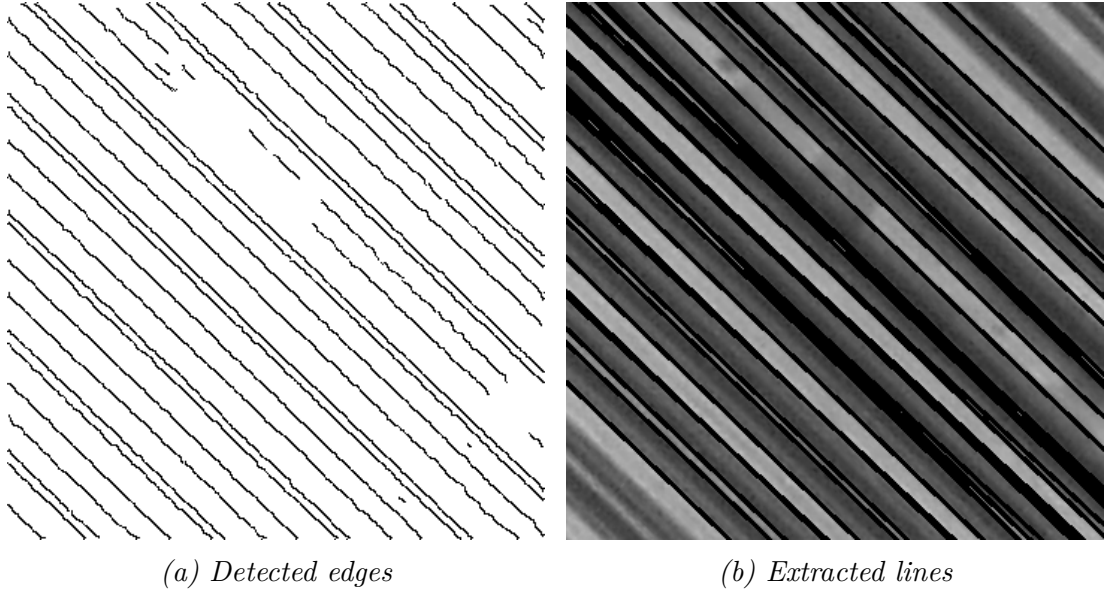
Figure 4.8: Hough Transformation with vote size = 120, represented by 4.8b, applied to image which edges can be seen in Figure 4.8a produced by Canny Edge Detector with a lower threshold set to 80 and higher to 110. The result is a set of lines where one edge is represented by multiple lines that slightly differ in angles.

$$\alpha_f = avg(\Theta)$$

We expect that the frame directions are mostly the same, therefore their median should give us a more accurate result since the average will include the outliers.

$$\alpha = median(\alpha_f) f \in F$$

This hypothesis was experimentally tested with conclusion that the median performs slightly better than using the average. The dominant direction α is then calculated as the median of of each f. Rotating each frame (not the central part) by the inverse angle of α results in all frames being vertically oriented.

Merging

At this point, all frames of the video show vertical FA. Each frame f is assumed to have a stripe of 50 px radius along X-axis which is unaffected by fish-eye effect (given Assumption 2). This part of each frame is cut out and merged.

Merging stripes and forming a single image was done in two steps. The first step was to form a skeleton by merging a stripe of every 50th frame e.g. 0,50,100 ... The 50 px tall stripes offers the best tradeoff between short ones, that create a jagged skeleton, and tall ones that are affected by the fish eye and stripes do not adjust well either. The selected stripes are one by one merged into a single image by the following stripes adjusting method. Given two stripes s_1 and s_2 that overlap in exactly one *ROW* (ensured by the cutting). The *ROW* where s_1 overlaps with s_2 is the bottom *ROW* of the stripe s_1 denoted b and the top *ROW* of the stripe s_2 denoted t. The goal is to shift t by Δx horizontally

so the difference between b and t is the lowest (if the frames would not be noisy, the lines would be almost identical). The Δx is found by maximizing the value of the following expression:

$$\sum_{x=1}^{W} b(x) * t(x + \Delta x)$$

The value of Δx is then used to shift stripe s_2 so it is aligned with s_1. The resulting image shows the whole FA with a high level of noise and visible transitions where the two stripes were joined together making the image unsuitable for defect detection. These artifact are removed in the second step where the rest of the stripes are merged into it — using the same method. Since the camera moves relatively slowly, every point of FA is captured in multiple stripes. Adjusting all remaining stripes to the skeleton gives us up to 49 intensity values (the top and bottom parts have less due to their limited neighborhood) for a single point on the skeleton. With the intensity from the skeleton, we can average all 50 values and than we can get the average intensity consequently reducing the skeleton's noise. The offset between the two stripes is given by the frame rate (29.2 for EasyPix and 25 for Olympus) and the speed of the camera in pixels (70 pixels per second). The offset is then calculated as $speed/framerate$. This method of noise reduction is justified by Assumption 4. The skeleton image and its noise free counterpart can be seen in Figure 4.9.

Cropping

The cropping removes the background of the image along with its adjusted sides, leaving just ROI of FA. The input uncropped OIO has solid background(see Assumption 5).The visual properties of the adjusted sides are different for the point-light and the tube-light. The comparison of the illumination was already discussed in detail in Section 4.2. The first step is to remove the solid background using RAIP. The plot of the derivation of input image RAIP (denoted R) shows the flat areas on the left and right sides of the function (see Figures 4.4b and 4.4a).

The left flat part is wide w px. The width w is calculated as the largest continuous interval where the difference of $R'(w) - R'(0)$ is less than $\frac{1}{3}$ of maximum of R'. The input image left part of width w is cropped. The solution tho the right side is symmetrical. The solid background removal is common for both types of illumination. Nevertheless, the procedure of the adjusted sides cropping differs for each illumination type in the following way:

Point-light: RAIP of point-light SG shows the flat areas that represent the adjusted sides to be removed (see Figure 4.4b). Cropping the adjusted sides is similar to the background removal in the previous step.

Tube-light: In case of the tube-light, SG have no such visual features. We do not use visual properties of SG but rather find the position of FR by their periodicity (see Figure 4.3a). The positions of the top left and top right rods are used to remove the adjusted sides. The periodicity of the rods can be seen in
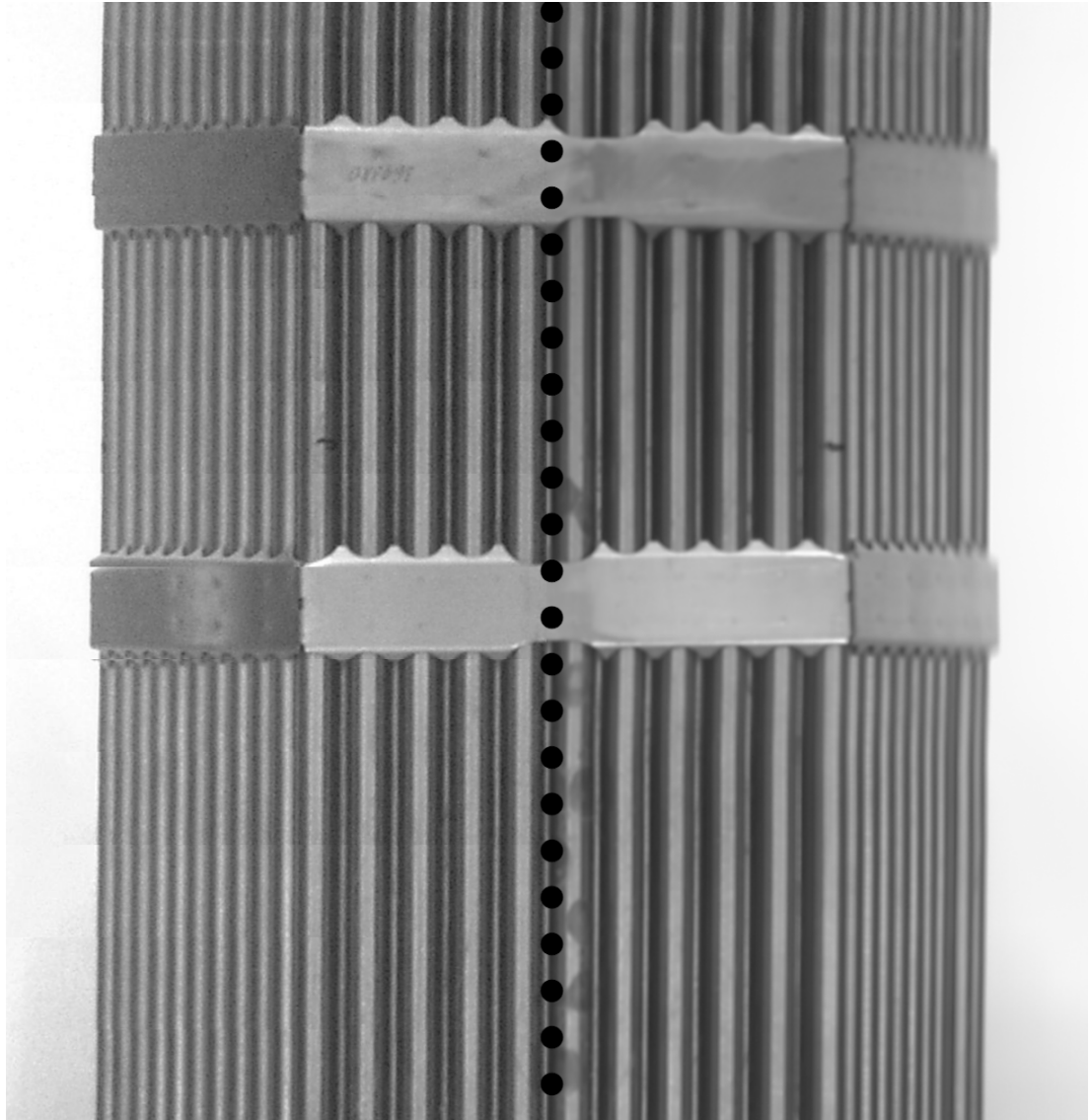
Figure 4.9: In the left half of the picture, we can see the skeleton which contains the same level of noise as the original video and noticeable transitions of the two joined frames (especially around spacer grids). In the right half, we can see the product of the merging of the remaining stripes - the noise free version. Due to neglects applied in the composition, the image is slightly blurred.
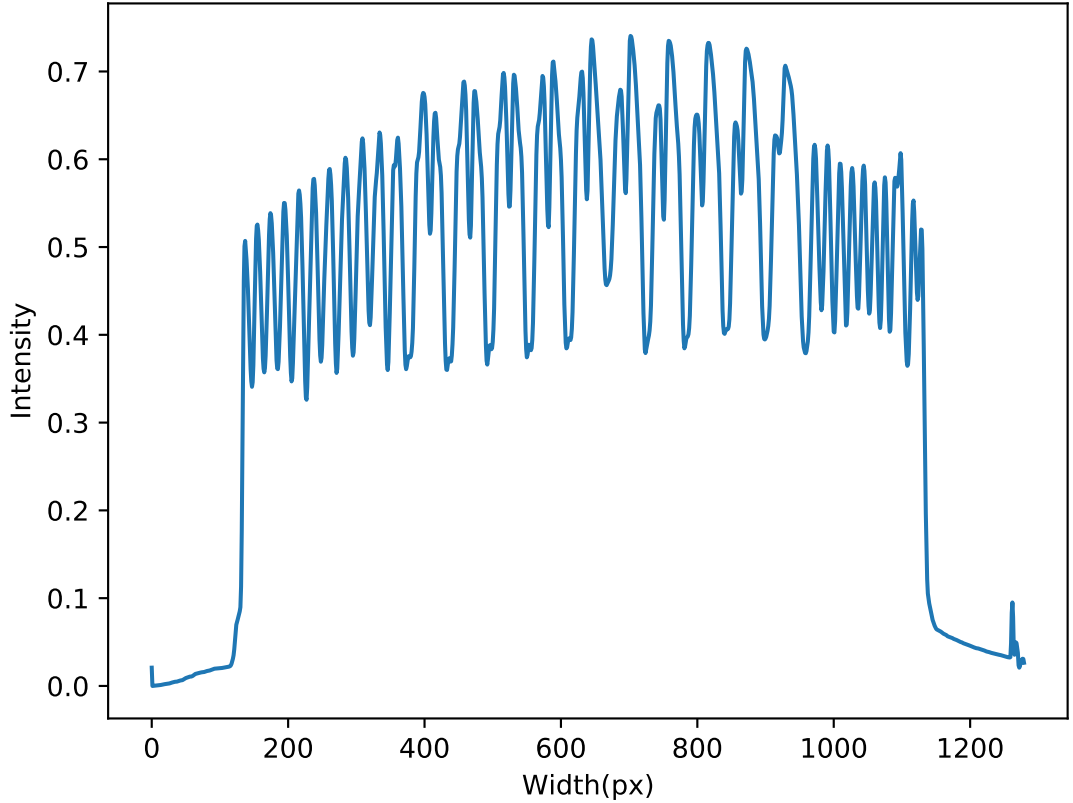
Figure 4.10: The plot of the rods profile RP which shows the peaks of the gaps between each two front-row rods. Can be only seen on the tube light videos.

the rods profile RP (see Figure 4.10) which is slightly different from RAIP. It is defined as follows.

$$RP(x) = max(RAIP) - RAIP(x)$$

Given Assumption 6, FA has exactly 11 rods so the signal is expected to have 10 equidistant peaks (each for the gap between since the peaks are upside down) $p_0 \ldots p_9$ in the central part of RP and a noise at the sides.

Some gaps show reflections that may disturb the signal periodicity. Those reflections are removed by applying the median filter (see Figure 4.11a) with width 100 px on RP which gives us MRP. On MRP, we find all candidates for gaps as peaks where the expected distance between two peaks is 70 px. We expect to find 10 peaks but in some cases, (e.g. severe defect, bad reflection) a different number of peaks can be found. If more candidates are found, we extract a part representing a single row (two peaks which distance is equivalent to expected width of a row, see Figure 4.11c) and use it as a kernel K for a convolution with MRP. This eliminates false candidates stemming from the adjusted sides rods (see example of such situation in Figure 4.11).

In case that fewer candidates are detected, we either interpolate the position of the ones missing (in case they are missing from the middle part) or we fill them from either left or right. According to Assumption 7 the position of the left or right peaks can lay in specified areas relative to the width of the image ($\frac{1}{10}$ to $\frac{1}{5}$). We prefer the candidate located closer to this position. The result is 10 peaks representing the gaps between 11 rods. We take the top left and top right gaps

(a) MRP

(c) Convolution kernel K

(b) Convolution result calculated
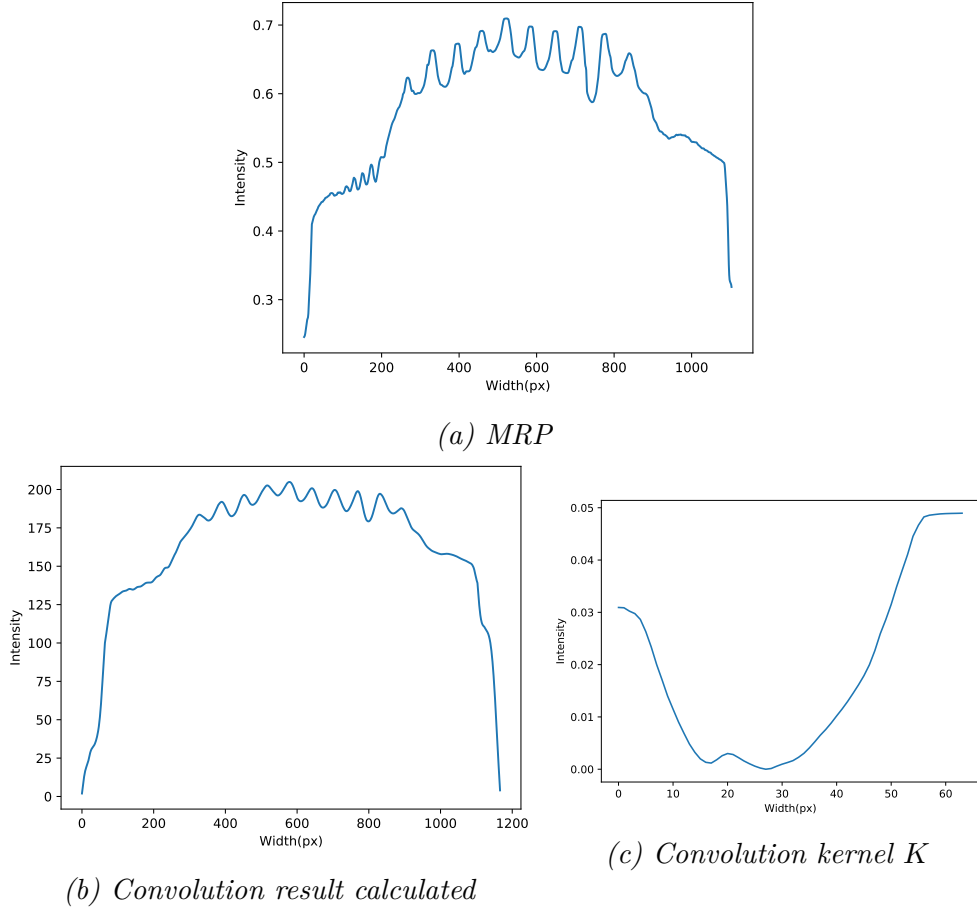
Figure 4.11: Convolution of MRP with a row eliminates false row candidates. On the right side of the MRP, we can see a small spike which is removed by the convolution (see Figure 4.11b).

locations, add a width of one rod and we found the boundaries of ROI.

Stage Result Evaluation

In this stage, OIO (see 4.12) was composed of the frames of the video. Each frame was rotated, cropped and used for the final composition in which subset of such frames were used to build FA skeleton onto which was the remaining frames blended.

The frame rotation normalization was done by calculating the average of dominant angles of individual frames and applying counter rotation. This approach was evaluated for all videos and the results were generally very good. The rotation was solved in the initial steps of the algorithms. The merging method greatly reduces the noise. It was revealed that the assumption about noise impact (see Assumption 4) and the fish-eye (see 2) were overstated since the image was blurred on the sides (that will get cropped) and slightly blurred across ROI. However, this does not affect the visibility of the spots much (they are still visible, see Figure 4.9) but small debris may disappear.

This step worked well on all videos with solid background but some videos were recorded without it. Due to the nature of the algorithm, the two subsequent frames failed to match, which disturbed the shape or the resulting OIO. The
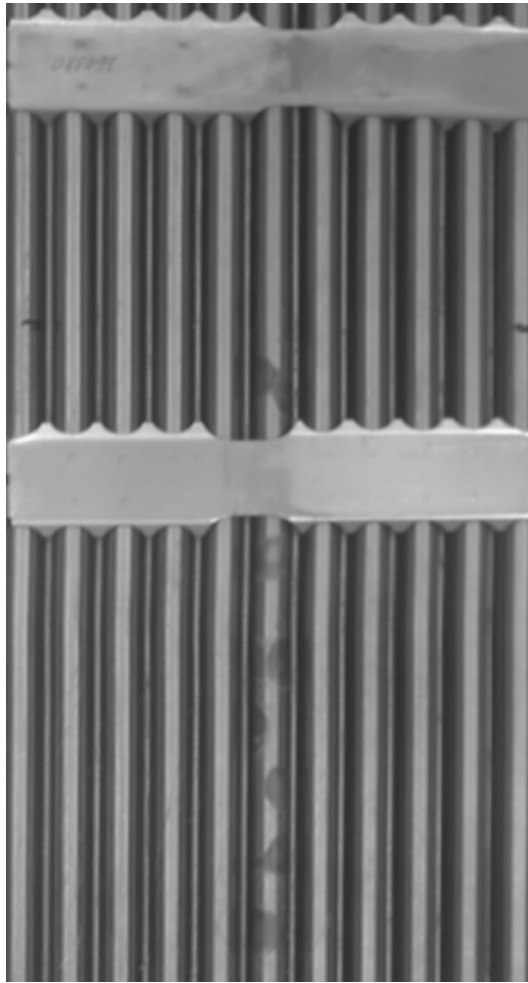
(a) Tube OIO
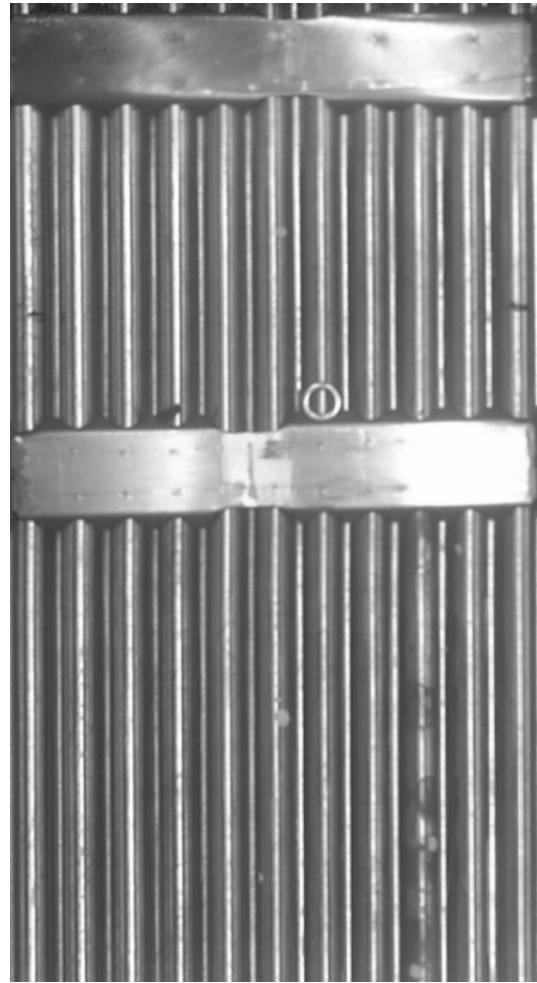
(b) Point OIO

Figure 4.12: The result of OIO construction stage looks apt for both types of light: tube-light 4.12a and point-light 4.12b.
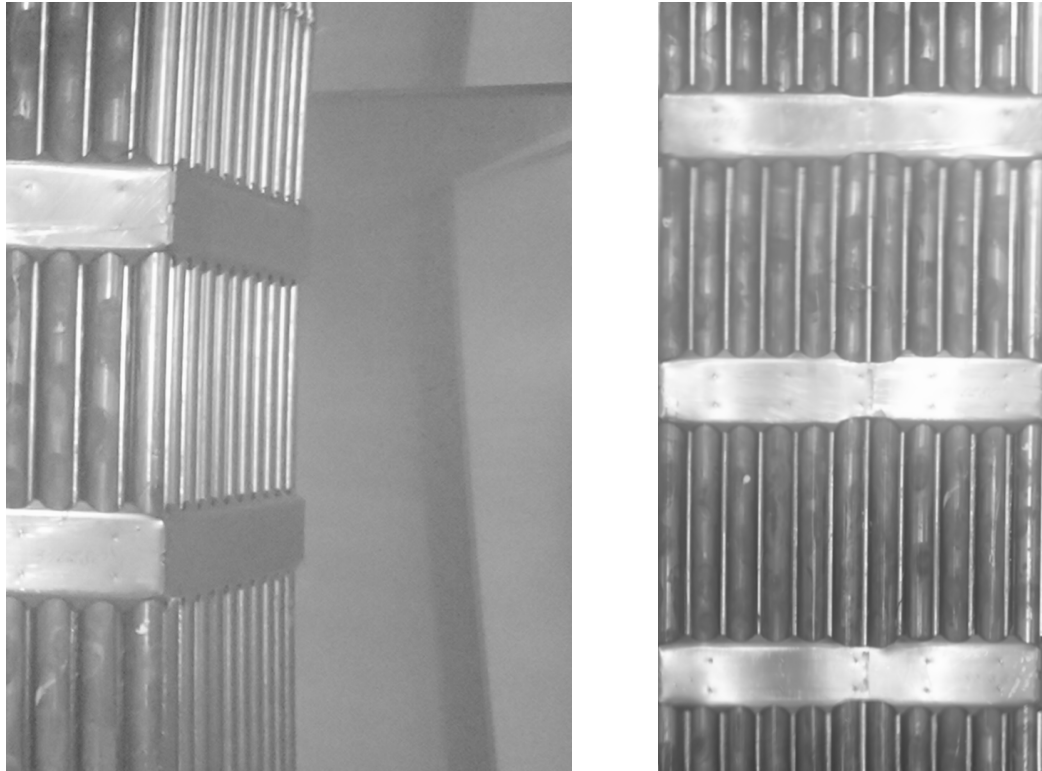
(a) Example Frame   *(b) Result*

Figure 4.13: The background of the example frame 4.13a causes problems in the matching of the subsequent frames. The problems can be seen in the resulting OIO 4.13b which rods are not straight nor sharp.

example frame of such a video and resulting OIO are presented in Figure 4.13.

Until this step, the method processes both illumination type in the same way. The first visible problems appear in the cropping of the adjusted sides. While cropping of the point-light image is straight-forward task (owing to visual properties of SG reflections) the tube-light image cropping represents more complex challenge.

The tube-light images do not have unique and significant visual feature. This has been bypassed with signal-processing techniques analysing periodicity of the signal representing the 11 frontal rods. This approach is less straightforward than in case of point light and the results can be distorted by an unexpected reflection. Some results shows OIO with few rods from adjusted sides and a half of a frontal rod missing (see Figure 4.14). This is caused by the fact that it is unclear from which side the missing part of the rod is supposed to be taken. Some efforts have been made e.g. decide the side according to the maximal derivation which worked only in around 90% cases.

In conclusion of this stage, the overall quality of the OIO was above expectation. The method overcame the downfalls of a video (such as the noise and camera-tilt) and furthermore produces image that has a potential to improve the process of inspection saving time of the inspector by removing the necessity of watching the video and looking at the picture instead.
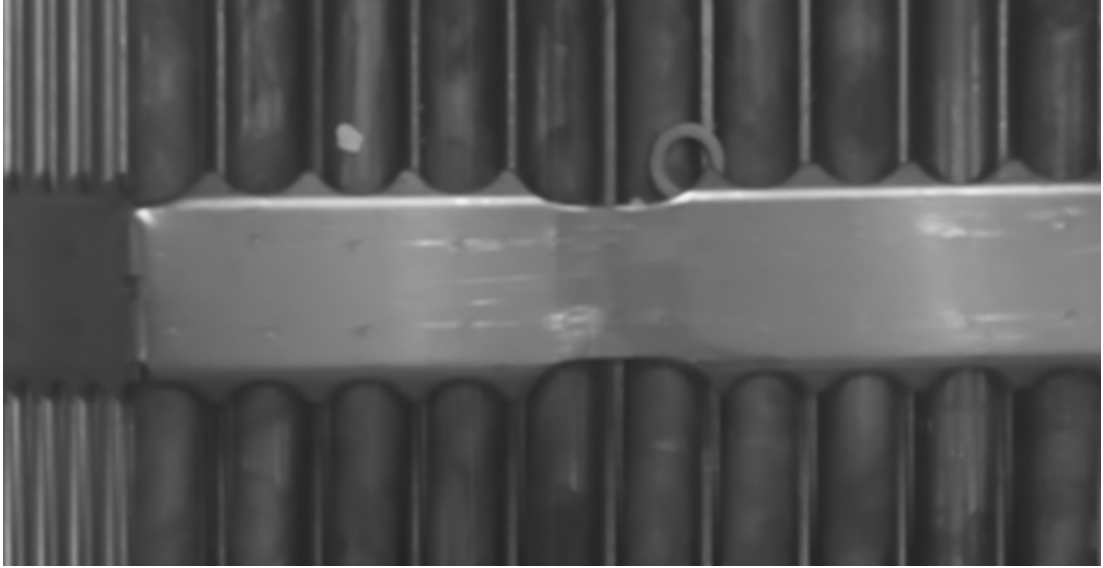
Figure 4.14: This example shows part of OIO where the two missing rods were filled from the wrong side.

4.5 Fuel Inspection

The goal of the inspection stage is to detect defects in OIO. The quality of this result depends on the quality of the input image. Assuming that OIO is correct, the following assumptions about it are made:

9. The defects covering the surface have visibly different (lower of greater) intensity than the surface without them. The defects must not cover the majority of the surface. The size and shapes of debris are not known.

10. The values of *ROW*s covering SG changes less rapidly than the *ROW*s covering FR. This fact can be illustrated by comparison of Figures 4.3a and 4.4a)

11. All SG are visually invariant by means of scale, shift and rotation and can be represented by one 2D raster mask.

12. OIO contains only fuel rods or SG e.g. when all SGs are identified and removed from the image, the reminder is FR.

13. Edges of SG teeth of SGs are assumed to be detectable by an edge detector.

14. OIO is not equally lit - the light across FA slightly changes from left to right and also from top to bottom.

Hypothesis: The defects can be detected by splitting OIO into multiple segments with either fuel rods or SGs. Each segment is then individually inspected for the presence of any anomaly with an algorithm specific to the segment type.
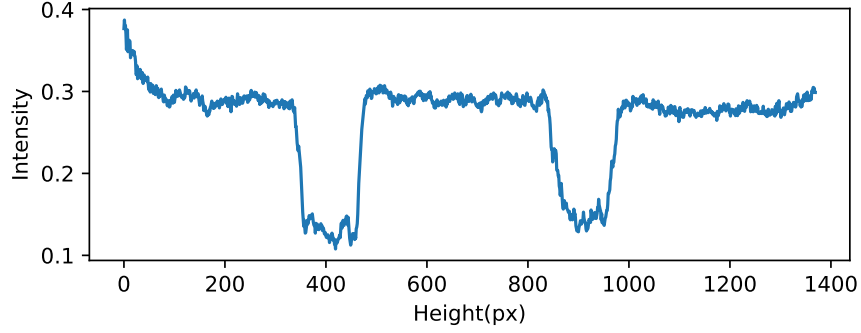
(a) CSIP showing clear segments with SG.
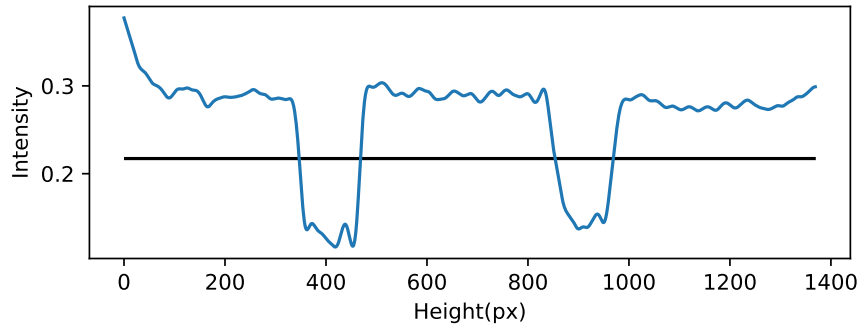
(b) The smoothed CSIP obtained from Butterworth filter with the order of the filter $N = 3$ and critical frequency $W = 0.08$ based on approximate offset of spacer grids. In our case t is approximately 70000. The horizontal line represent the threshold separating the position where SGs appear

Figure 4.15: Results of operations performed to find boundaries of spacer grids

OIO Segmentation

The vertical coordinates of SGs on the input OIO are approximated by searching for continuous intervals of high values in CSIP. Such intervals represent the top and bottom sides of a SG bounding rectangle. The border separating rods from SG is established by fitting a handmade mask. Furthermore, regularization techniques to tackle imprecisions are applied based on illumination quality and variability of SG.

Spacer grid rectangular boundaries localization: Since SG is mostly flat we assume that values of overlaying ROWs change less than the values of FR ROWs (see Assumption 10). To locate SGs, we calculate OIO' by differentiating OIO along x axis and then calculate its CSIP. The result is shown in Figure 4.15a. We can clearly distinguish between the parts with rods and the ones with SGs.

Some, especially the point-light videos have less readable profile due to the reflections on SG. Their effect is mitigated by Butterworth filter [9] which smooths the segment intervals. The approximate location of spacer grid is revealed by thresholding the signal. The threshold is computed by K—means algorithm with $k = 2$. The result can be seen in Figure 4.15b. This way we found top and bottom of SG grid bounding rectangle but it does not contain the whole SG so we extend it by 20 px on both sides.

Spacer grid mask fitting: According to Assumption 11 all SGs are similar to each other. The goal is to use the handmade 2D raster mask (see Figure 4.16) and try to find the best fitting location on in the area limited by the rectangular boundaries found in the previous step. SG in the boundaries can be slightly rotated ($\pm 7.9°$ is tolerated). The fitting needs to be tried in the location and the rotation as well. Due to the sharp reflections on the teeth edges that optically reduce SG area we had to create the mask slightly smaller to improve the accuracy of the location and compensate for it in the next step.
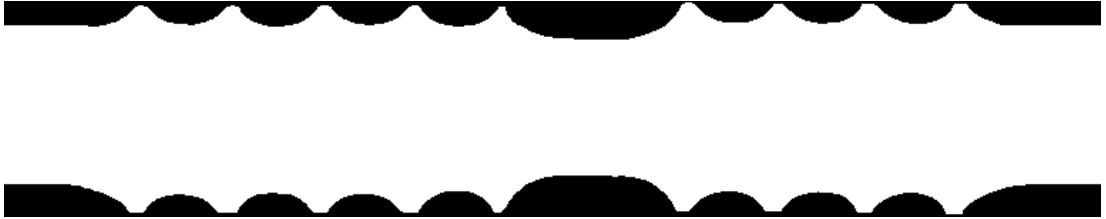
Figure 4.16: The 2d mask used in the segmentation process.

The surface of SG is flat, therfore its values should vary less than surface of the rods. Due to that, the best approximate position of the mask m is found by minimizing the score s for different rotations computed as a sum of RAIP derivatives of a spacer grid segment s_i masked out by mask $m_{x,y}$ placed at (x, y) coordinates.

$$s(x, y) = (\frac{\partial s_i}{\partial x}) * m_{x,y}$$

Spacer grid border refinement: Assumption 11 proved to be too strong. Initially, we presumed that the mask is misplaced due to the reflections and shadows concealing the real borders. We tried to improve it with additional border refinement.

The borders of the SG found in the previous step did not precisely represent its real borders because the mask is slightly smaller. The real borders are supposed to lay few pixels away. To curb the imprecision of mask fitting and to find the real borders, they are expanded and refined in the following way.

The first step is to establish and area where the real border is expected to lay. This is done by applying slightly larger mask with the same rotation and scale. The borders may lay in the area of the greater mask but outside of the smaller mask. In such area Canny Edge detector (see Figure 4.17) is applied to highlight all edges. Because of Assumption 13 the edges of teeth are revealed.

The edges of SG are more likely to have debris stuck inside. In the image, a piece of debris like a short wire can be just 1-2 px wide. For this reason it is important to precisely find borders between FR and SG. The SG edges in the picture span over multiple pixels but the edge detector extract only 1 px, therefore the resulting border may be jagged. Since the shape of the teeth is known, it is possible to refine its shape by ensuring that the transition between subsequent teeth is convex. Such property is ensured by shifting each pixel in vertical direction into the best possible position. This produces rough curve that is smoothed by applying Active Contours [10] (see Figure 4.18). The refined SG segments are then subtracted from OIO, splitting it into multiple FR segments.

(a) Tube-light spacer grid

(b) Tube-light detected edges

(c) Point-light spacer grid

(d) Point-light detected edges
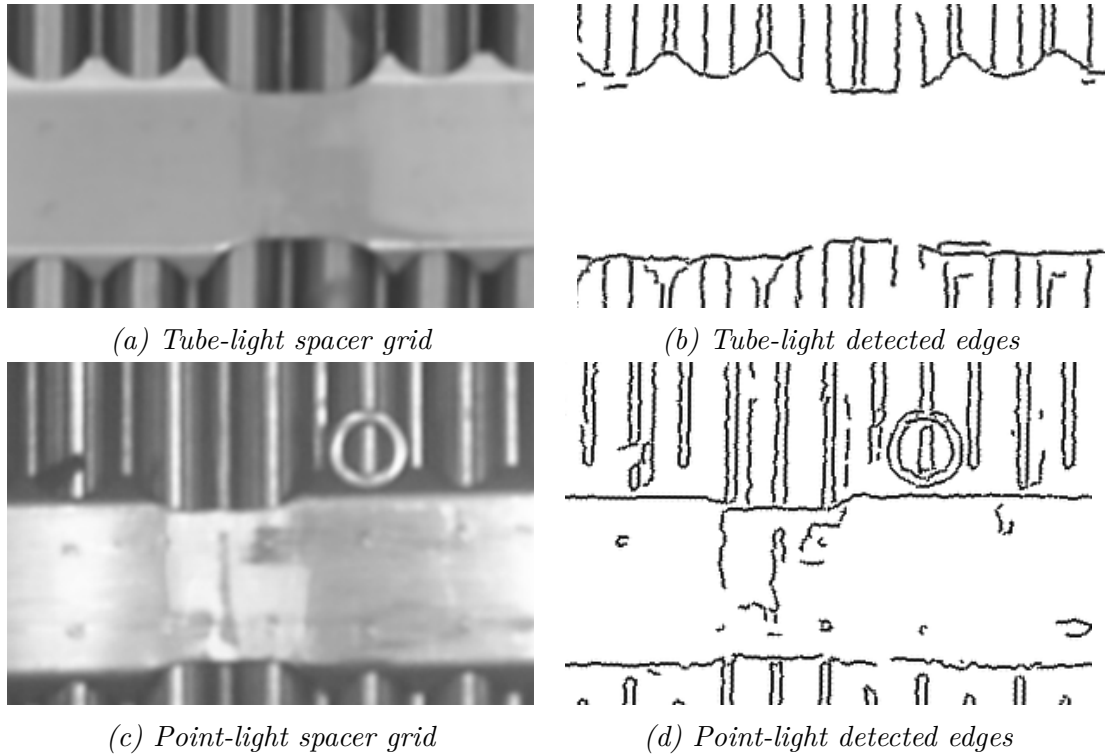
Figure 4.17: The tube-light teeth edges 4.17b detected in the part of the spacer grid 4.17a. As was demonstrated, the edges 4.17d does not show on the point-light images 4.17c even with a different edge detector parametrization
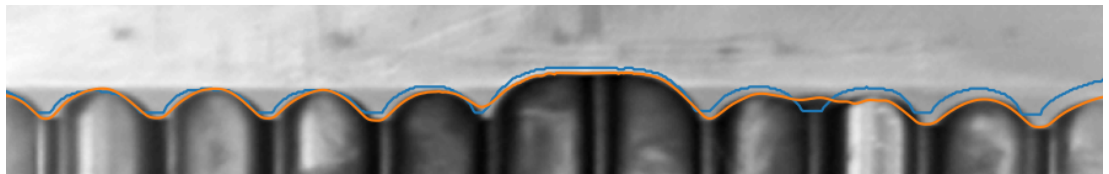
Figure 4.18: The mask border is shown as a blue line and the refined edge as orange. We can see that refined border is much more precise yet still not perfect. This approach did not work at all on point light videos.

The final result is a set of FR segments and a set of SG segments that can together create one large segment mask.

Anomaly Detection

The defects are anomalies in otherwise well-defined environment. They are revealed for each segment separately by computing an approximation of defect-free image and measuring the difference from the original one. The result is a heat map where all anomalies can be observed. The shapes and sizes of debris had not been known in advance (see Assumption 9). The properties of oxides (white spots) are known but they are not required for the algorithm to reveal them. In the end, all defect heatmaps are composed together (since they represent only one segment) forming a defect heatmap of the original OIO.

Fuel rods anomalies: The detection of anomalies on fuel rods relies on the fact that the rods are totally straight (ensured by OIO composition algorithm). For each FR segment we predict a defect free version. Each defect-free FR segment i-th *ROW* is calculated as RAIP of the *ROW*s $i - k$ to $i + k$ where k denotes the size of the neighborhood (in our case we used 10). The step for a single line is visualized in Figure 4.19.
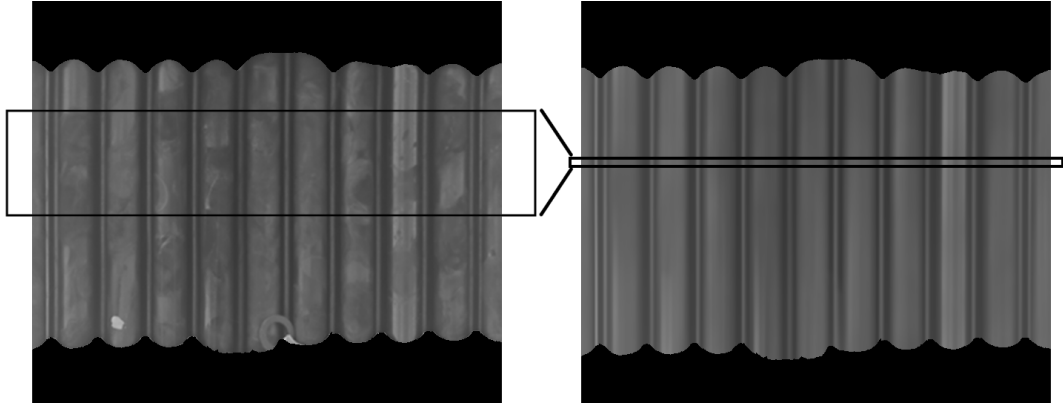
Figure 4.19: Defect free FR is generated using sliding windows algorithm that calculates each ROW of the defect free image as RAIP based on the immediate neighborhood of the line in the original FR segment. The figure shows an example of the neighborhood used by one ROW. The black areas on the top and bottom are not involved in the calculation.

Assumption 9 ensures that the original FR segment does not have a significant amount of defect. It would undermine reliability of the defect free version which would not embody the anomalies and consider them a standard. In the calculation, we used sliding window because the light across FA is not uniform and changes in both vertical and horizontal directions (see Assumption 14). Using only one "defect free *ROW*" calculated form the whole OIO would not work.

The difference between the original FR segment and its defect free version is then measured by subtracting the the defect-free from the original image. Each step is visualized in Figure 4.20.

Spacer grid anomalies: SG anomaly detection is based on the same principle. Additionally, given the horizontal nature of SG construction, the defect free SG utilized the horizontal direction as well. The resulting heat map is then computed by subtracting S from original SG segment. This step was not used in the final solution due to its direct dependency on the discarded borders-searching algorithm. The result of the SG defect detection is presented in Figure 4.21.

Stage Result Evaluation

In the inspection stage, the input OIO was split into multiple segments of two classes: fuel rods and spacer grids. The anomalies of each segment were then extracted to a heatmap. In the end all heatmaps were composed into a single large heatmap where each pixel of the heatmap corresponds to an unexpected intensity change of the respective point of OIO.

The segmentation step finishes with precisely separated rods from SG, e.g. each pixel of OIO belongs to either rod segment of SG segment. This task was
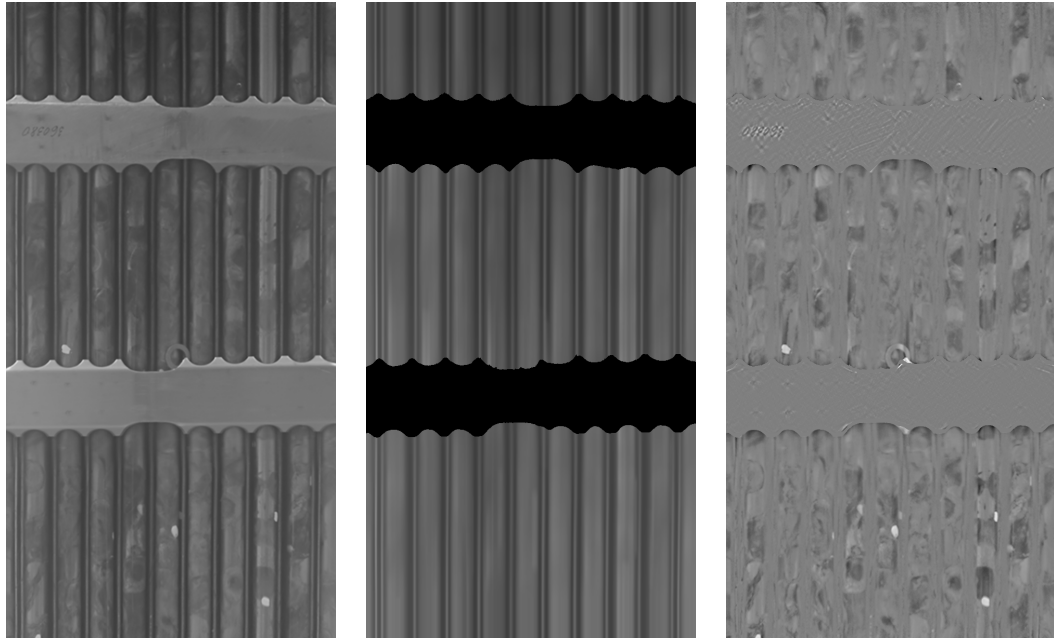
(a) Original FR segment with defects

(b) Defect free FR segment

(c) FR segment defect heatmap

Figure 4.20: The original segment 4.20a is used to predict a defect free image (without SG) 4.20b. The difference between the defect-free segment and the original one is shown in the heatmap 4.20c.

well-defined but, on the contrary to final results, its difficulty proved to be underestimated. Its initial assumptions were based on geometrical properties of a single SG and on the visual properties shown on the tube-light videos. The fact that masks are not similar and the amount of reflections and shadows on the point-light videos increased the complexity to the task beyond expectation. Due to the limited time, instead of redesigning this process completely, we decided to improve the existing algorithms.

When it was revealed that the mask does not fit all SG we made it smaller and implemented border refinement algorithm. In some cases, the refined border was tens of pixels away from the expected position. To limit the area where the border can lay we added one more mask; larger than the original one which border demarcated outer border for the algorithm. This improvement did not impact the results much; therefore we added one more step. We implemented regularization where we tried to utilize well-known shape of the teeth and try to fit it to the edges of SG. Additionally, the bad segmentation influence the results of SG defect detection which also did not perform well.

In the end, after the discussion with the CVR inspector we decided to take a step back, enable this feature only for high-quality videos and disable it for the others. We also added a step where each SG with bounding rectangle is saved for manual inspection. This decision was accepted because the SGs typically require more attention than the rest of FA.

The anomaly detection of rods performed well in all images. With the segmentation feature enabled, SG borders inaccuracy caused false positives. The problem with uneven light of the tube-light videos was solved by calculating de-
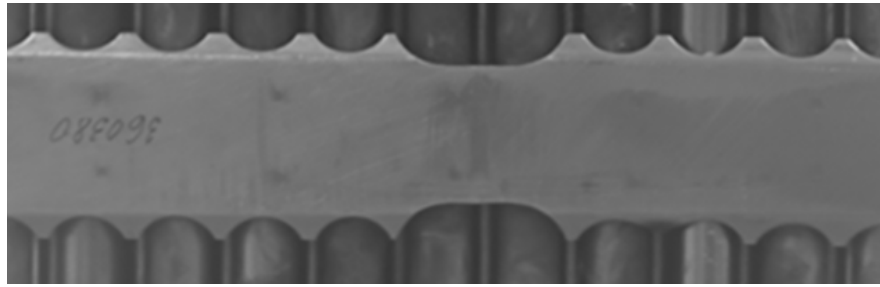
(a) Original spacer grid
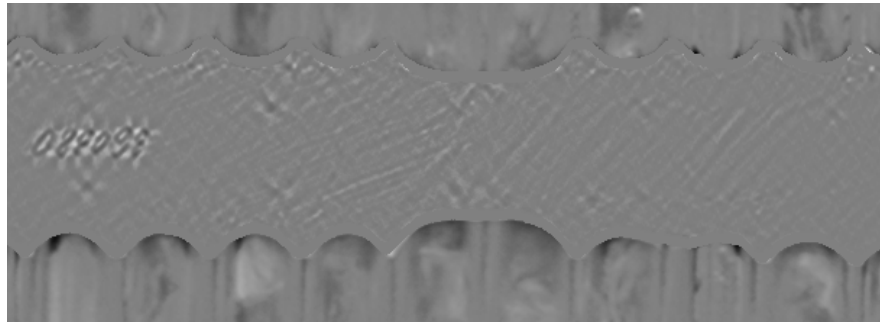
(b) Defect heatmap without border refinement

Figure 4.21: The defect heatmap 4.21b of the spacer grid 4.21a visualise the probability of defect on the surface. We can see that the most probable defect is the engraving followed by bumps and scratches. The spacer grid is outlined with solid-gray area at the top and bottom. This area is demarcated by the xor of two mask. This crucial area represents a place where the SG border should lie. However, the white spots on around the outline suggest that the outline does not cover the SG precisely and the imprecisions are considered anomalies. Since SG extraction was not included in the final product, the surface of the SG was also absent and is shown here to asses the results.

fect free image using the sliding window. This step needs caution. The defect can be missed when the sliding window size is smaller than the defect - it will be integrated into the defect free image instead of standing out in its surrounding. We did not come across any defect, that would be missed - therefore no advanced algorithm was under consideration.

Spacer grids are more prone to artifacts caused by bad illumination. Some of them have engraving, slight bumps or other visible irregularities (as was shown in Figure 4.21b) which are not defects. All of them are detectable on the heatmap which lowers confidence of the results. The original assumption about SG visual properties did not hold true in the real dataset.

4.6   Defect Visualization

In the OIO construction stage, we created OIO which is used for quick overview of FA condition. In the inspection stage, we calculated the heatmap representing anomalies which is not particularly comprehensive on its own. In this stage, the original OIO is combined with the anomaly heatmap resulting in OIO with the most severe defects highlighted. Note, that the heatmap created in inspection stage is deconstructed into the original segments which are then separately used for visualization.

In this stage, the following assumption is used:

15. Any point on the segment heatmap with value belonging to the bottom 0.3% or the top 0.3% is considered a defect.

All anomalies representing possible defects lies in the top or bottom extremes (see Assumption 15) of each segment individually. This assumption is based on empirical research of the inspector to favour false positive to true negatives.

Procedure: The values that are not considered anomalies are removed by thresholding.

The last step is to color the values of the heatmap, the greatest values by orange color and the lowest by blue [11]. The color map of each segment is then laid over the original OIO. The result is visualized in Figure 4.22.

Stage Result Evaluation

The visualization stage combined OIO and the anomaly heatmap into a single image. OIO with visualized anomalies is used as the evidence in the reports filled after the inspection finishes. The decision whether a highlighted anomaly is a defect still rests upon the inspector. Hence, the fact that false positives can occur is not an issue. The form of OIO with highlights was satisfying to the inspector.
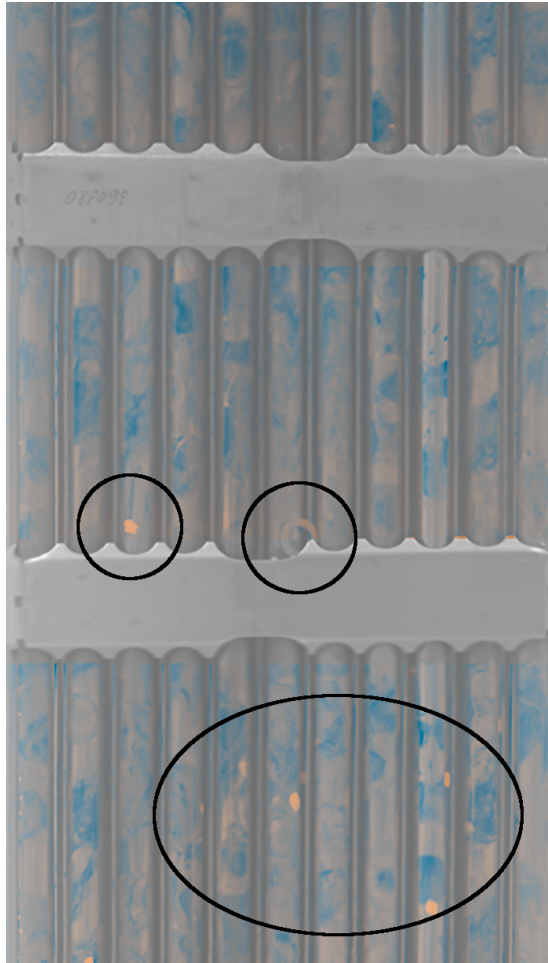
Figure 4.22: The defect heatmap created in the inspection step is thresholded and combined with OIO to highlight defects. We can see that all defects has been revealed (see the encircled area). The picture also shows false positive, which was expected due to the nature of the algorithm.

5. Discussion and Future Work

The discussion evaluates the results of FDDM and exemplifies some assumptions held during the development process (see Section 5.1). In Section 5.2, it suggests changes that can improve the quality of the current results. The impact of the project is discussed in Section 5.3. The future work and project development directions are discussed at the end of the chapter in Section 5.4

5.1   Results Evaluation

FDDM was applied on the whole dataset consisting of videos of various types of light and quality, not only in the latest. Their properties vary due to the gradual improvement of illumination, camera or camera-stand (as discussed in Chapter 3). The illumination type proved to be significantly more impactful than originally anticipated and the pipeline handled each type separately. The construction of OIO proved to be robust enough to handle the insufficient quality of the point-light videos influenced by the shadows or sharp reflections. OIO was composed correctly, with both types of videos without significant difference in the quality, the cropping rarely experienced some issues with missing side rods.

The segmentation struggled to extract the precise borders of the SG. The assumptions related to construction properties of SG were too strong. For example, we determined that the level of SG border detectability is disrupted by the the point light more than originally anticipated. When the point light is shed on the spacer grid it creates too sharp reflections on the top border, making the teeth and their surrounding appear almost solid white, which prevented the edges to be detected. Conversely, the bottom border was very dark, the edges blurred and undetectable as well. Even though an extensive effort was made to suppress the negative impact of the point light in the scene development and to improve the methods of segmentation, we revealed that this approach does not yield satisfying results and this problem requires reconsideration. Due to the fact that SG always requires additional attention, it was acceptable to extract all SGs with their bounding box and present them to the inspector separately for closer inspection. The final project contains the segmentation feature but it is enabled only for the high quality data.

FDDM is semi-automatic tool for defect detection, helping the inspector to notice all the defects and optimize process of report making. Due to the exploratory nature of this project, no metric for precision evaluation was formalized. In cooperation with CVR, we have developed one which suits well the semi-automatic nature of the FDDM. The metric counts the number of detected defects relative to the number of defects found in the fuel rods segments. Due to the nature of the tool, the false positives are acceptable therefore not used in the metric (they are filtered out by the inspector). These spacer grids were also omitted - their evaluation requires individual inspection. FDDM, with minor tweaks, was used in the videos from the real inspection with satisfying results. The videos are visually similar to the experimental one with few extra properties: the videos were zoomed in on few rods discarding the need for cropping and each corner of FA was covered by an angle piece concealing two rods on each side.

5.2 Improvements

When we talk about improvements there are three types of them:

1. Improvements of the quality of the screening process

2. Covering of edge cases of the current assumptions

3. Corrections of assumptions and suggestion of new algorithm

So far, we have struggled with hard reflections of point-light videos. We tried to eliminate them by pouring milk into the water tank and installing light diffuser to spread the light more evenly. Such improvements helped in OIO composition but some reflection affecting the OIO segmentation still remains. The screening process improvement, such as this, should eventually lead to having the quality of point-light videos as close as possible to the tube-light.

The segmentation process worked well for majority of the tube-light videos. But in case of the point-light ones, FDDM underperformed due to the strong assumptions. One such issue was with cropping the background, where the point-light videos significantly differ from the tube-light and had to be handled separately, or with cropping out the adjusted sides, where some rods could be missing. With the strong assumptions, we did not manage to segment OIO reliably and inspect defects on the SG. Under these assumptions—segmentation and SG assumptions still remain open, since the videos have a lot of edge cases we did not manage to cover all of them. We could cover them with additional effort.

The alternative to additional improvement of the current methods would be to reassess the assumptions. The current methods are based on the assumptions made from the process of the screening and FA construction properties. The OIO composition assumptions hold true for all the videos but the assumptions of the segmentation do not. It may be beneficial to introduce a different assumptions and redesign this stage completely.

5.3 Project Impact

The project was limited to three month during which FDDM was designed and applied to the inspection videos (supposedly similar to the real ones). The quality of the videos gradually improved based on the feedback from FDDM results. Conversely FDDM was gradually adapted to cover specifics of new videos. Additional success of this project, apart from developing FDDM, was that the videos recorded in the experimental facility were visually close to the videos of the real inspection.

Reflections, especially the ones on metallic alloy, are a common problem in image processing field therefore FDDM needs to be prepared to tackle them. In this case, any reflection suppression in the screening process will greatly improve the results with less effort than designing more robust method. The following aspects of the screening process improved:

- New camera bought - The resolution and image quality improved, yet shaking appeared due to the introduction of a heavier camera.

- Camera-stand reinforced - The shaking was reduced to minimum

- Point-light hard reflections reduced - After multiple experiments, the water in the water tank was mixed with milk and a diffuser was installed on the light attached to the camera.

In conclusion, FDDM can reliably turn videos from FA screening into OIO and additionally highlight all the defects. During the development, we explored a possible solution to SG extraction. We were successful in the extraction of it in good light condition (under tube-light) yet it remains an open problem since the result of point-light videos were unsatisfactory. The extraction was concluded with a observation that the proposed algorithm is build on too-strong assumptions hence the segmentation still remains an open problem.

5.4 Future works

Checking FA for surface defects is not the only goal of visual inspection. The other is to measure and monitor construction defects (bending and twisting). Such defects are common but if left unchecked they can result in a complications. For example, bent or twisted FA prevents insertion of a control rod which can lead to partial loss of control over the chain reaction. The construction defects are measured manually during the inspection. This tedious and time consuming activity can be automatized as well. For such improvement, further effort in implementing already well-defined procedure is required.

Visual inspection results are compared across multiple sessions to get insight into the processes in the reactor. This project can be improved further by adding a defect properties classification feature. This will allow for tracking the changes of individual defects in time and possibly a prediction of the defect development.

The most significant shortcomming of FDDM is the fact that it requires videos with no interruptions. This requirement would mean great changes to the well-established inspection process. To avoid that, OIO composition could be re-designed to handle the interruptions. With additional effort, this could also be improved to work online, so that the inspector would not have to move with the camera back or rewind the video, the already-recorded part would be in the OIO.

To date, the inspection process utilizes only a single camera. Nowadays, it is common to use multiple cameras at the same time. The company Ahlberg Cameras [1] offers the system of multiple cameras with the dedicated light source. Employing multiple cameras at once will allow inspector to overwatch the screening of multiple faces of FA at the same time and closely inspect the defects afterwards with the help of OIOs.

---

[1]https://www.ahlbergcameras.com/

6. Conclusion

This thesis is based on the project focused on application of image processing methods in nuclear fuel visual inspection. We presented an algorithm that automatizes reporting of nuclear fuel visual inspection. The algorithm utilizes an edge detector, Hough Transformation, registration based on convolution maxima and signal filtering for output image cropping. The most significant benefit is the transformation of the inspection video into a one image overview saving the time required for re-watching the video during report filling. Additionally, this image has defects highlighted so the inspector can check that all defects were noticed.

While examining the results, we have encountered some issues as well. Image cropping can be improved to cover 100% of videos. Segmentation of OIO should be redesigned due to huge variability of light conditions.

In conclusion, we have managed to automatize report making and a detection of spots and debris to the satisfaction of the inspectors from CVR. With slight changes to the screening process, we developed the method that helps inspector to double-check all defects and generates materials used in the reports. The project was finished within three months, at the end of which, after experimenting with real data, the project was applied to real data and inspectors were satisfied with the results.

Appendices

A   Cameras Parameters

The parameters of cameras Easypix GoXtreme Race Mini and Olympus IM005 are presented in Table 1.

	Olympus IM005	GoXtreme Race Mini
Product type	Digital camera	Sport camera
Image resolution	Up to 4000 x 3000	Up to 2592x1944
Video resolution	840x2160 @ up to 30 fps 3840x2160 @ up to 25 fps 1920x1080 @ up to 60 fps 1280x720 @ up to 120 fps	640x480 @ 60 fps 1280x720 @ 30 fps
Image pickup device	1/2.3" CMOS	CMOS
Lens	Olympus lens 4.5 to 18.0 mm f2.0 to f4.9	F3.1 f=9.3mm
Shutter speed	4 to 1/2000 sec.	n/a
Monitor	3.0"	1.77"
Dimensions	113.0x66.0x31.9 mm	67x48x29 mm
Weight	250 g (including battery)	48 grams
Exposure	±2	±2
Waterproof	yes	yes

Table 1: Table showing parameters of two cameras used in this project

B   Videos

Throughout this thesis, we used figures that originate from one of the following videos. The videos are attached to this thesis (see Attachement B.4).

B.1   Tube Light - EasyPix Action Camera

This video was taken by Easypix Action Camera under the tube-light at the very beginning of the project. It represents the category of videos used to develop the first prototypes of OIO composition and segmentation. The results of FDDM applied to this video can be seen in Figure B.1

B.2   Point Light - EasyPix Action Camera

This video was taken by Easypix Action Camera as well but under the point-light at the very beginning of the project. Videos of this category were used to test and improve robustness of the prototypes developed for the tube light
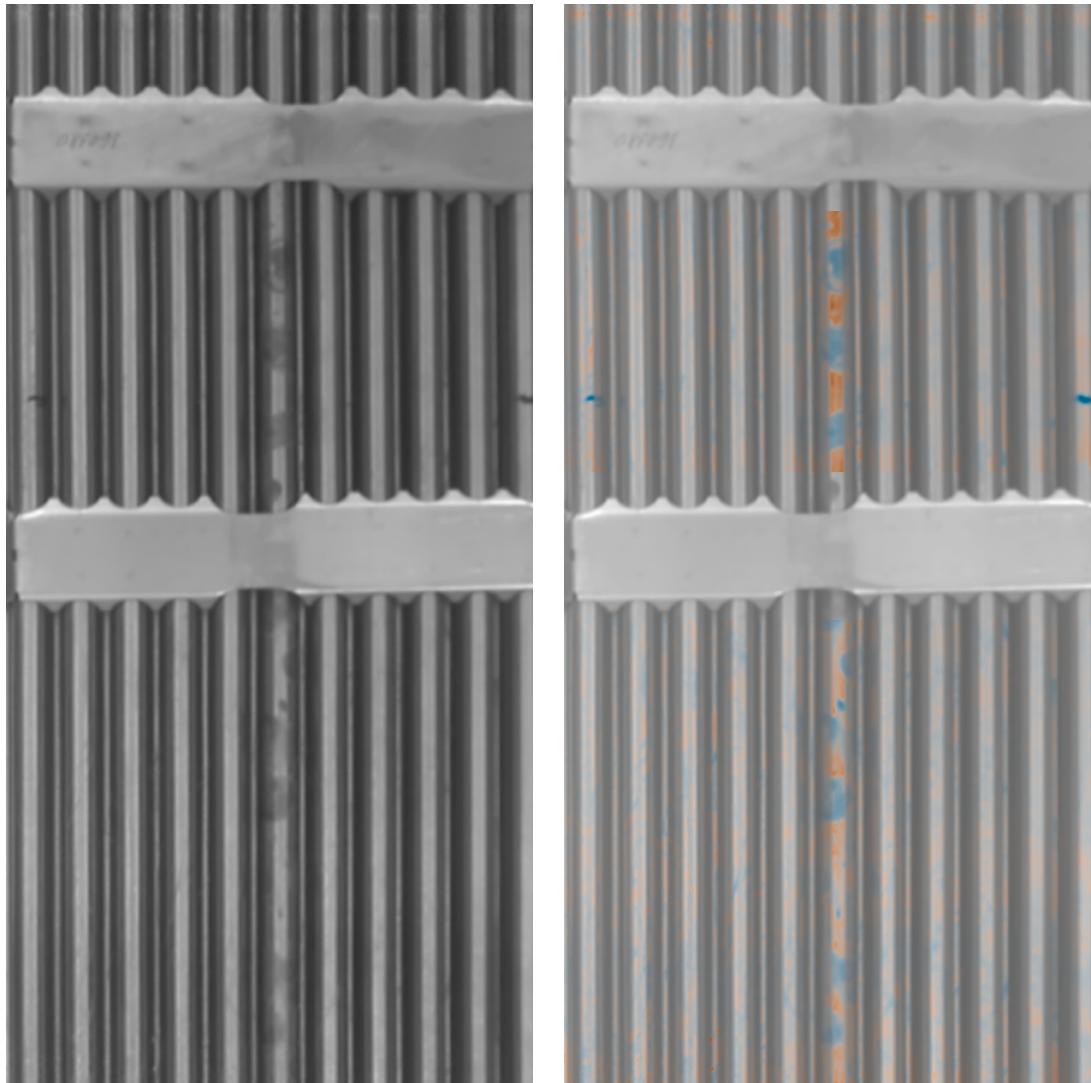
(a) OIO   (b) Highlighted defects

Figure B.1: Tube light illuminated FA captured with EasyPix Camera

type described in Section B.1. The results of FDDM applied to this video can be seen in Figure B.2.

(a) OIO　　　　　　　　　*(b) Highlighted defects*
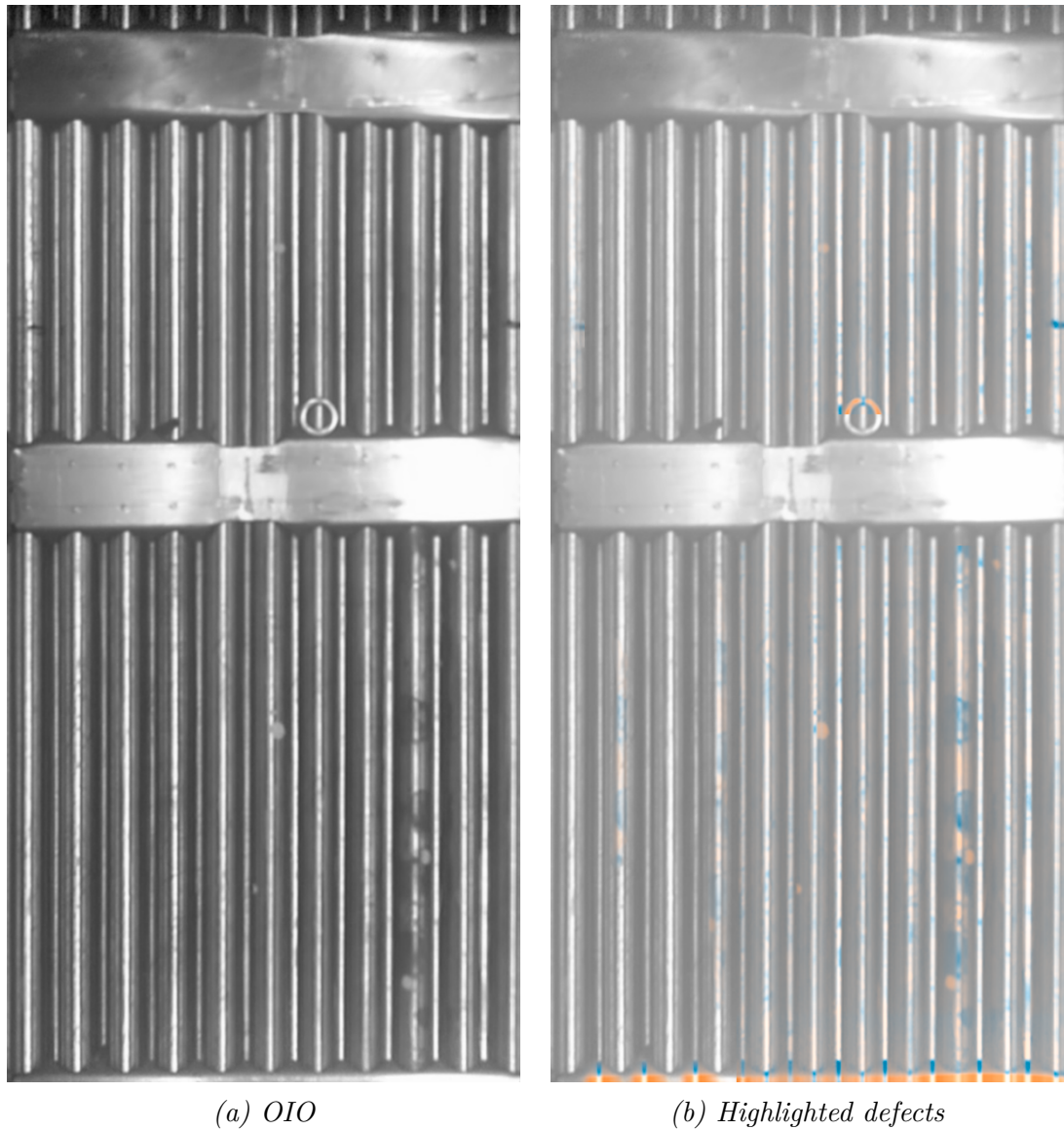
Figure B.2: Point light illuminated FA captured with EasyPix Camera

B.3　Tube Light - Olympus Camera

This video represents the highest quality videos, it is recorded with Olympus Tough under the tube-light. It has the best visual properties of all recorded videos. Applied on this video, all methods work the best. The results of FDDM can be seen in Figure B.3

B.4　Point Light - Olympus Camera

At the end of the project, the point-light videos were significantly improved. Compared to the video described in Section B.2, the reflections are much less sharp and the darker areas are better observable. This major improvement of the
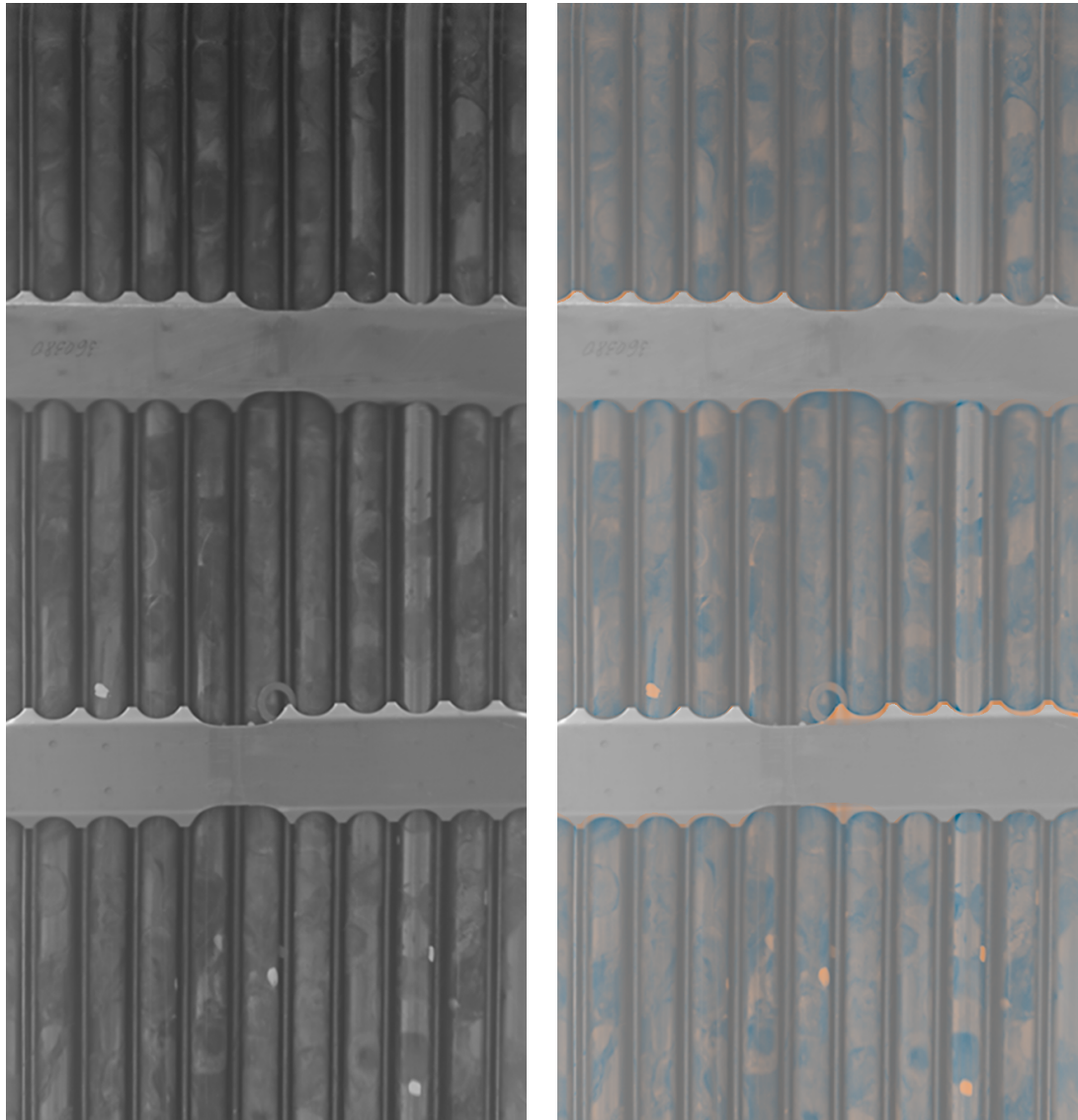
(a) OIO *(b) Highlighted defects.*

Figure B.3: Tube light illuminated FA captured with Olympus Camera. You can see that the teeth of SGs (see B.3b) are highlighted implying that the SGs were not omitted. That is because this image is considered high quality one and was used for the refined segmentation. The SG defect inspection remained disabled though.

video quality can be attributed to usage of the new camera as well as application of a diffuser. The results can be seen in Figure B.4
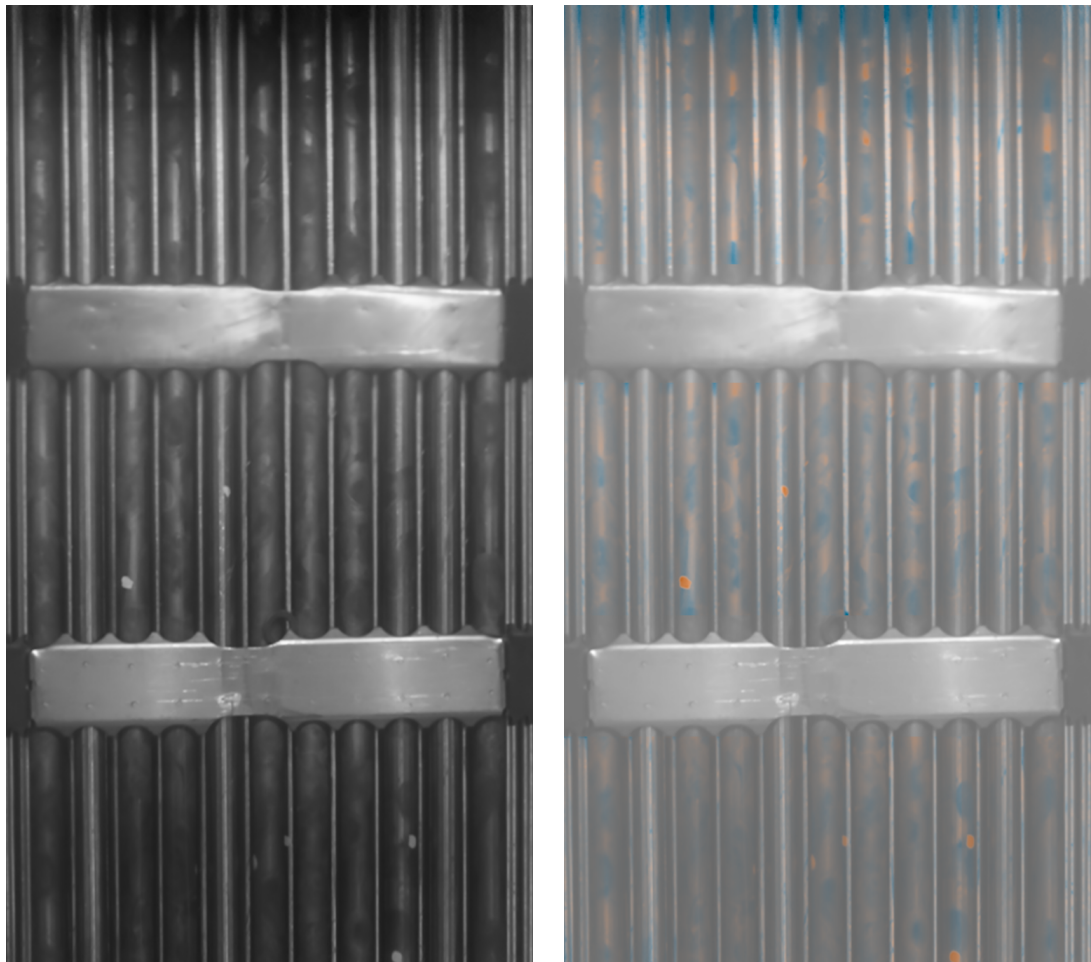
(a) OIO   *(b) Highlighted defects*

Figure B.4: Point light illuminated FA captured with Olympus Camera.

Bibliography

[1] Arthur Watkins, Dennis Kunerth, and Timothy Mcjunkin. Eddy current examination of spent nuclear fuel canister closure welds. 2006, 01 2006.

[2] Martina Mala. Post-irradiation inspections on tvsa-t fuel assemblies at temelín npp. *VVER 2013*, 2013.

[3] Martina Mala. Seven years of inspections on tvsa-t fuel assemblies at temelin npp. 12 International conference on WWER fuel performance, modelling and experimental support, Bulgaria, 2017.

[4] D Markov, V Smirnov, A Smirnov, Sergey Perepelkin, and V Polenok. Integration of post-irradiation examination results of failed wwer fuel rods. *4th International Conference WWER Fuel Performance, Modelling and Experimental Support*, 01 2003.

[5] Martina Mala and Marek Miklos. Nuclear fuel inspections and repairs at the temelin npp. *Bezpecnost Jaderne Energie*, 19(11-12):362–365, 2011.

[6] Zhangpeng Guo, Zhiwang Wu, Sheng Liu, Xuan Ma, Chaoyi Wang, Dijiao Yan, and Fenglei Niu. Defect detection of nuclear fuel assembly based on deep neural network. *Annals of Nuclear Energy*, 137:107078, 2020.

[7] Yongzhi Min, Benyu Xiao, Jianwu Dang, Biao Yue, and Tiandong Cheng. Real time detection system for rail surface defects based on machine vision. *EURASIP Journal on Image and Video Processing*, 2018(1):3, 2018.

[8] P.V.C. Hough. Method and means for recognizing complex patterns. 12 1962.

[9] S. Butterworth. On the theory of filter amplifiers. *Experimental Wireless and the Wireless Engineer*, 7:536–541, 1930.

[10] Michael Kass, Andrew Witkin, and Demetri Terzopoulos. Snakes: Active contour models. *IEEE Proc, on Computer Vision and Pattern Recognition*, 1:321–331, 01 1988.

[11] J. Blažek, B. Zitová, and J. Flusser. Image fusion for difference visualization in art analysis. In *2013 Digital Heritage International Congress (DigitalHeritage)*, volume 1, pages 653–656, Oct 2013.

List of Figures

List of Tables

Attachments

Video

- old_tube.mp4 (described in Appendix B.1)

- old_point.mp4 (described in Appendix B.2)

- new_tube.mp4 (described in Appendix B.3)

- new_point.mp4 (described in Appendix B.4)